To the Graduate Council:

I am submitting herewith a thesis written by Robert L. Perrin entitled "The Effect of Surface Condition on Aqueous Corrosion and Environmental Embrittlement of Iron Aluminides." I have examined the final copy of this thesis for form and content and recommend that it be accepted in partial fulfillment of the requirements for the degree of Masters of Science, with a major in Metallurgical Engineering.

R. A. Buchanan

R. A. Buchanan, Major Professor

We have read this thesis and recommend its acceptance:

Charles R. Brooks

E. S. Starkey

Accepted for the Council:

Associate Vice Chancellor
and Dean of the Graduate School

The Effect of Surface Condition on Aqueous Corrosion and Environmental Embrittlement of Iron Aluminides

A Thesis

Presenteed for the

Master of Science

Degree

The Unversity of Tennessee, Knoxville

Robert L. Perrin

August 1996

DEDICATION

I would like to dedicate this thesis to my parents, Luther Perrin and Anita Perrin, for all of the years of support and encouragement they have given. They allowed me to pursue my dreams to get a higher education and gave me the strength to keep going.

I would also like to dedicate this thesis to Erica Vaught who was there for me when I really needed it. Her support helped me deal with all of the problems that are associated with research and helped me keep focused so that I would trudge through all of the set backs.

ACKNOWLEDGMENTS

The author would like to express his thanks to his major professor for the opportunities he provided as well as all of his guidance and time. The author would also like to acknowledge the advice of his thesis committee--Dr. E. E. Stansbury and Dr. C. R. Brooks.

The author would also like to acknowledge the help of the machine shop in Dougherty Engineering for their help in precisely machining sample for testing.

This research was sponsored by U. S. Department of Energy, Fossil Energy AR&TD Materials Program, under contract DE-AC05-84OR21400 sub-contract 11B-07685C-T92. The author would like to thank many people at the Oak Ridge National Laboratory, Metals & Ceramics Division, for their support and advice.

ABSTRACT

This research was focused on the effect that surface condition has on the aqueous corrosion properties and environmental embrittlement of iron aluminides. All tests were performed in a mild acid chloride solution [pH=4, 200 ppm Cl^-] that simulates severe atmospheric exposure. Cyclic anodic polarization tests were performed to determine susceptibility of different surface conditions to localized corrosion. These tests indicate that the as-processed and furnace oxide surfaces performed poorly in comparison to the mechanically cleaned and chemically cleaned surfaces. U-bend tests were conducted to see how either a 750°C oxide surface or a mechanically cleaned surface affected hydrogen embrittlement. At E_{corr} neither surface condition produced cracking in the U-bend specimens. At the hydrogen charging potential of -1500 mV SHE, the FAL-Mo, FA-129, and FA-84 U-bend specimens cracked but only in the mechanically cleaned surface condition. Slow strain-rate tests were conducted to get a quantitative understanding of the effect that surface condition has on hydrogen embrittlement. For all tests (either at E_{corr} or at -1500 mV SHE) the percent total plastic elongation was greater for the oxide surface specimens than for the mechanically cleaned samples. This in conjunction with the U-bend results indicates that the furnace oxide on the surface of the specimens provides some protection from hydrogen penetration and thereby retards hydrogen embrittlement effects.

TABLE OF CONTENTS

LIST OF TABLES

TABLE PAGE

LIST OF FIGURES

I. Introduction

Research on iron aluminides began in 1934. However, little attention was given to iron aluminides because of their low ductility. Recently, extensive work has been performed at Oak Ridge National Laboratory to increase the room temperature ductility and strength of iron aluminides. There also has been a great deal of effort put towards increasing the high temperature strength. The overall goal for these materials is to produce a low-cost, low-density intermetallic alloy based on the Fe_3Al stoichiometry for use in advanced fossil energy conversion systems. This requires optimum combinations of strength, ductility, and corrosion resistance. These alloys are being considered for applications where more expensive stainless steels or nickel based alloys are being employed. Examples of such applications are steam turbine parts, heating elements, components for highly oxidizing molten salts, sulfidizing environments, furnace fixtures, and gas-clean-up filters (1).

Other studies have focused on the effect of alloying additions on the properties of iron aluminides. High temperature tensile strength and creep strength have been shown to improve with the additions of Ti, Mo, Zr, Hf, or Nb. However, all of these additions gave increases in high temperatures properties at the expense of room temperature ductility (2). Additions of several of the aforementioned elements together gave synergistic effects regarding metallurgical properties, but the complexity of their exact effect becomes more difficult to determine (2).

Despite the extensive work done towards determining mechanical properties, much less has been done to determine the aqueous corrosion properties of these alloys. Therefore, a range of alloy compositions were considered and tested to determine their corrosion properties at room temperature. Work has been done to evaluate the corrosion properties of iron aluminides in electrolytes with pH values ranging from strongly acidic to strongly basic. The electrolytes also evaluated the corrosion resistance as a function of chloride concentration. Tests have also been performed which study the synergistic effect of stress and corrosion on the properties of iron aluminides (3).

The high temperature properties as well as room temperature corrosion properties of iron aluminides have been studied. However, the room temperature corrosion tests were performed on iron aluminides with clean surfaces. No study has been performed to determine what effect the service oxides on the surface have on the room temperature corrosion properties. High temperature service creates oxides on the surface that are dramatically different from the oxides formed on the surface of a sample cleaned of such oxides. The alloys used for this study were supplied by the Oak Ridge National Laboratory and are designated FA-84 (Fe-28Al-2Cr-0.05B, at. %), FA-129 (Fe-28Al-5Cr-0.5Nb-0.2C, at. %), and FAL-Mo (Fe-28Al-5Cr-1Mo-0.04B-0.08Zr, at. %), FA-385 (Fe-35.65Al-0.20Mo-0.05Zr-0.11C, at. %), and FAP-Y (Fe-16.1Al-5.4Cr-1.1Mo-0.1C, at. %). These alloys are commonly produced by arc-melting 500 g specimens in a water-cooled copper crucible in a chamber backfilled with argon. They are remelted six times for homogenization and then drop cast in a copper mold to form ingots. The ingots are then

hot-forged 50% at 1000°C, hot-rolled 50% at 800°C, and warm rolled 70% at 650°C to a final thickness of 0.75 mm. (4). It is the purpose of this study to evaluate the effect of differences in the surface condition on the aqueous corrosion and environmental embrittlement of iron aluminides.

II. Literature Review

2.1. Materials

Intermetallic iron aluminides based on Fe_3Al and FeAl have been developed at the Oak Ridge National Laboratory. These alloys offer good high-temperature oxidation and sulfidation resistance as well as low material cost. They offer many of the advantages of stainless steels with the added advantages of lower density and lower usage of strategic materials such as chromium. However, their use as structural materials has been limited by low room temperature ductility and a drop in strength above 600°C (2).

Iron aluminides are targeted for applications that currently employ either nickel-based alloys or high-nickel-content steels with the addition of one or more of the strategic elements Cr, Co, Nb, Ta or W to achieve high temperature oxidation resistance, high strength with adequate ductility, fabricability, and thermal stability. These alloys are expensive and do not have the desired characteristics for high temperature components in advanced fossil energy systems due to their lack of resistance to hot corrosion in environments containing SO_2, SO_3, H_2S, and alkali sulfates(3). An added advantage of iron aluminides is their lower density ($\rho = 6.6$ g/cm^2) when compared to steels and nickel based alloys ($\rho \approx 7.8$ g/cm^2).

The iron aluminum phase diagram is shown in Figure 1 (5). It shows that the intermetallic compound, Fe_3Al, is present between approximately 20 and 35 atomic percentage aluminum. Figure 2 shows the phases present on the iron aluminum phase

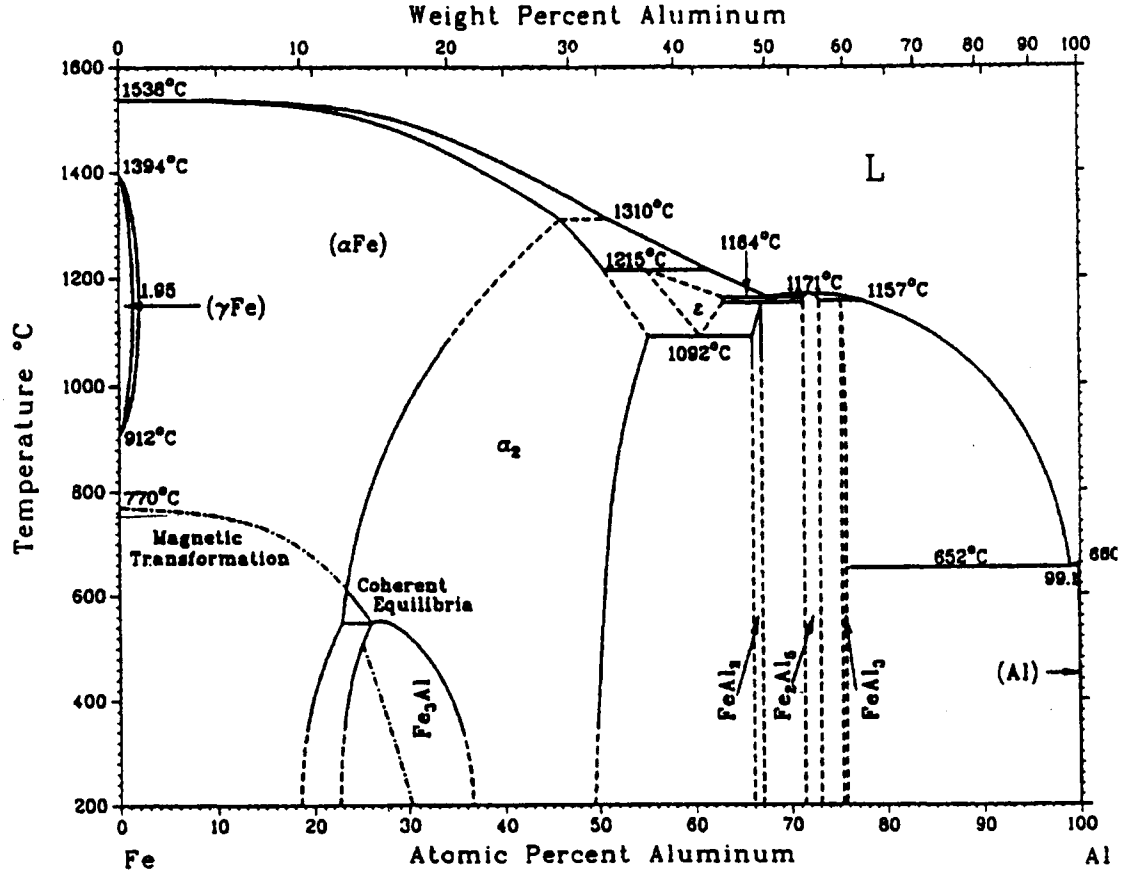

Figure 1: Iron aluminum phase diagram (5).

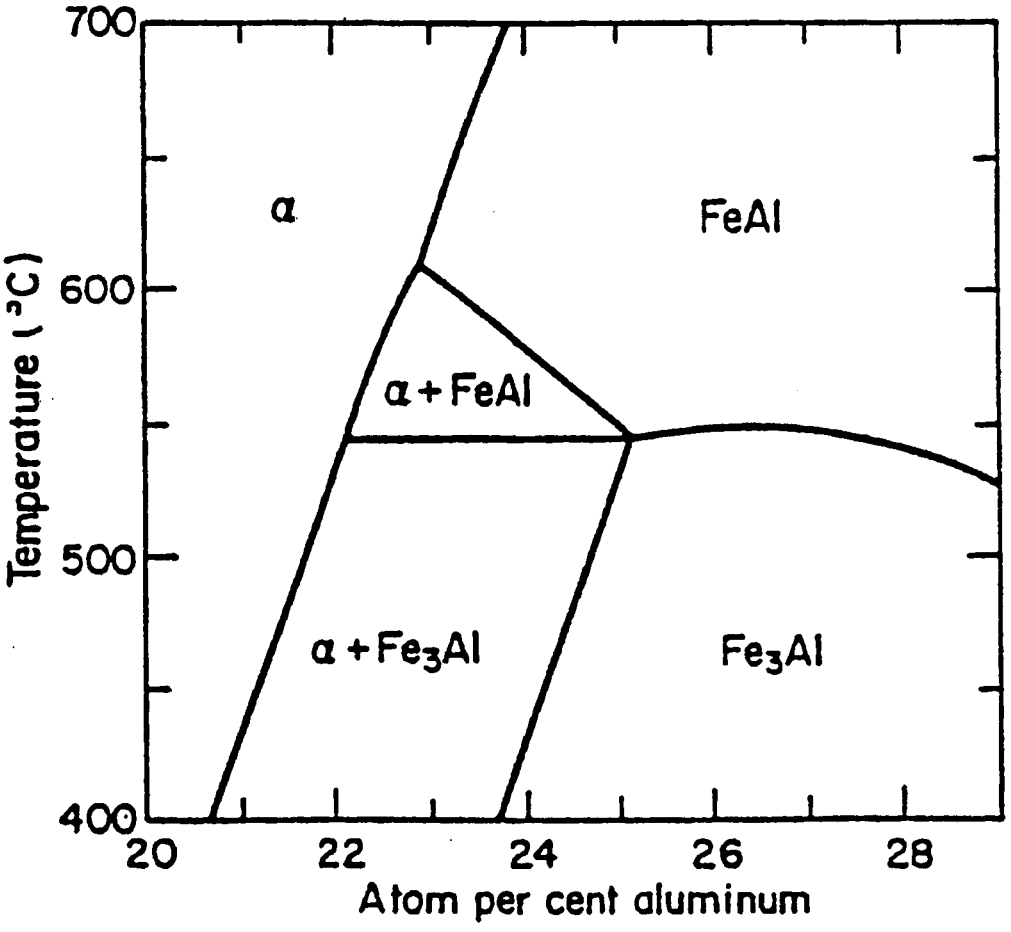

Figure 2: The coherent iron aluminum equilibrium phase diagram (6).

diagram between 20 and 30 atomic percent aluminum in more detail (6). It can be seen that at temperatures above 550°C FeAl is the stable intermetallic compound. There is a major stoichimetric difference between these two intermetallics as well as a crystallographic one. Fe_3Al has an ordered $D0_3$ structure while FeAl has the imperfect B2 ordered structure (2). Figure 3 shows both the $D0_3$ lattice and the B2 lattice. $D0_3$ and B2 are both structures which are BCC type ordered superlattices. B2 is designated as α_2 on the phase diagram while $D0_3$ is shown as the Fe_3Al. The transition from both the ordered $D0_3$ and the disordered α solid solution to B2 is a second order transformation (7), (8).

The B2 lattice is preferred to the $D0_3$ lattice because the B2 treatment can greatly improve both room temperature ductility and strength (9). It is known that poor room temperature ductility is caused partly by dynamic hydrogen embrittlement (2). This is demonstrated by the fact that iron aluminides are intrinsically ductile when tested in a dry oxygen atmosphere at room temperature (10). However, the $D0_3$ structure loses most of its ductility during hydrogen charging (6.4% to 1.6%) whereas the B2 structure only partially loses ductility (16.8% to 9.4%). The key concerns for environmental sensitivity lie in the morphology and structure of the grain boundaries. The B2 thermomechanical treatment (hot forged 50% @ 1000°C, hot rolled 50% @ 800°C, warm rolled 70% @ 650°C to a finish thickness of .75 mm) affects the morphology in that the processing deforms the grains into a pancake shape which is parallel to the surface of the sheets (9).

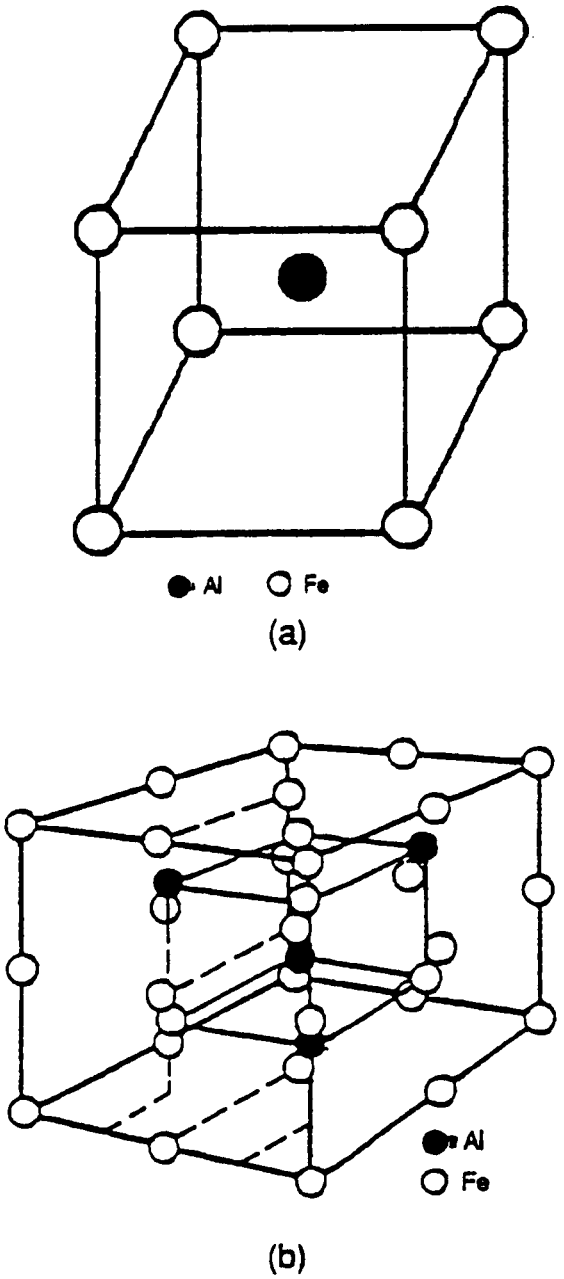

Figure 3: Ordered crystal structures of iron aluminides: (a) FeAl (B2), and (b) Fe_3Al (4).

This morphology does not provide a path for hydrogen to easily diffuse into the material.

Hydrogen embrittlement is not solely responsible for low ductility. Another reason for low ductility is the lack of operative slip systems to allow cross slip. This allows grain boundary decohesion because the inability to cross slip prevents spreading of slip across the grain boundary, resulting in a brittle, intergranular fracture (11).

For iron aluminides to find usage in a wide range of applications, the room temperature ductility and strength above 600°C will have to be improved. Work at Oak Ridge National Laboratory has shown that additions of up to six atomic percent chromium can remarkably improve both room temperature ductility and high temperature strength. Chromium is beneficial in that it modifies the surface-oxide rather than affecting the bulk properties. The change that chromium has on the surface oxide would tend to indicate that there is a change in oxide chemistry that makes it more resistant to hydrogen penetration and thereby reduces hydrogen embrittlement (12).

Improvement in room temperature tensile strength and ductility also can be gained by controlling the heat treatments. Figure 4 shows the effect that annealing temperature has on the total elongation at room temperature for FA-129. It shows that the room temperature ductility is maximized at a temperature of 750°C. Figure 5 shows the effect of annealing time at 750°C for FA-129. It indicates that annealing time is not as critical for room temperature ductility as annealing temperature (13). The heat treatment used for these alloys is therefore one hour at 750°C in air followed by an oil quench to protect the iron aluminide from moisture during cooling and to freeze in the B2 ordered structure.

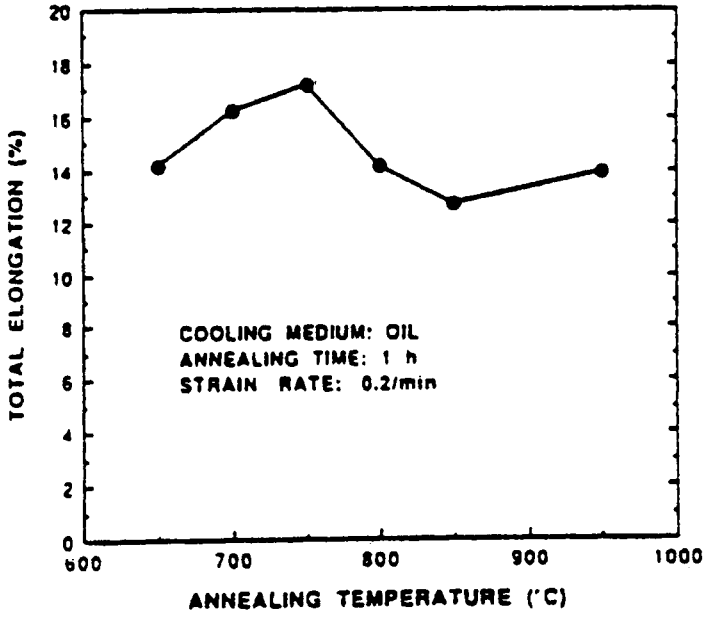

Figure 4: Effect of annealing temperature on room temperature total elongation of FA-129 (3).

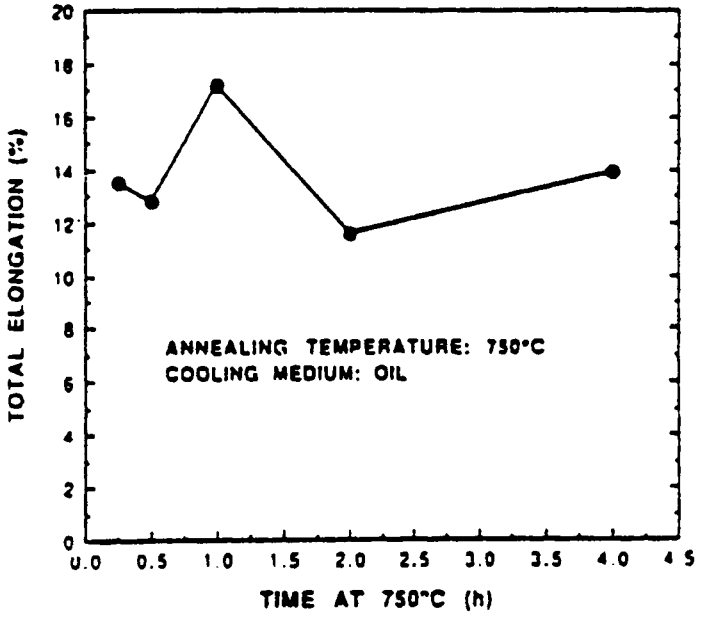

Figure 5: Effect of annealing time at the maximum ductility temperature on the room temperature total elongation of FA-129 (3).

A study of the properties of alloys of 24 to 30 atomic percent aluminum has shown that the most promising composition for further development is Fe-28Al. Figure 6 shows the room temperature tensile properties for these alloys as a function of aluminum content. The maximum yield strength was found in binary alloys with 24 to 26 atomic percent aluminum. The percent elongation increased with increasing aluminum content. The optimum amount of strength with percent elongation is at the intersection of the two lines at 28 atomic percent aluminum (14).

2.2. Pitting Corrosion

Metals and alloys that are resistant to uniform corrosion are generally susceptible to another type of corrosion, localized corrosion. Of particular interest here is pitting corrosion. It is controlled by the formation and maintenance of a thin film of passivating oxide on the metal surface. For the oxide to be a viable passive film it has to be thermodynamically stable in the environment to which it is exposed and adhere to the surface of the metal. If it flakes or is unstable, then it will expose the base metal to further corrosion.

Pitting corrosion occurs in metals and alloys where the passive film is viable. There is usually some type of breakdown of the passive film that allows the service environment to attack the base material. The breakdown of the passive film and propagation of the pitting mechanism is as follows:(15) (3) Pitting initiation takes place with a small change in the electrolyte composition at the metal-solution interface. The halides in the solution

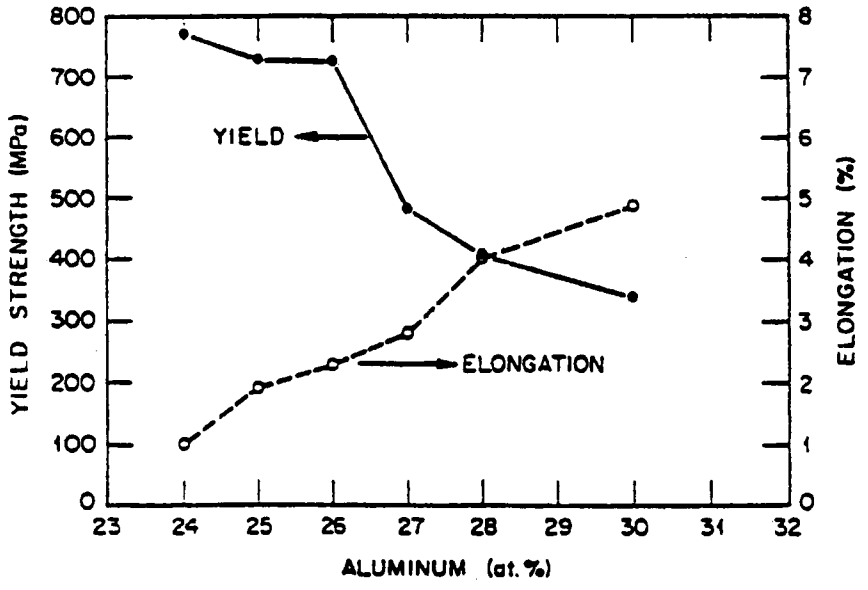

Figure 6: Room temperature yield strength and elongation versus composition of iron aluminides (3).

can be absorbed into the passive film surface around a lattice cation. This will form a transitional complex that will be of high energy and which can immediately separate from the oxide ions in the lattice. This will remove the passive film from a portion of the base material and leave it exposed to the environment.

The single charge transfer will take place by the following anodic reaction:

$$Me \Rightarrow Me^{n+} + ne \qquad (1)$$

This dissolution reaction is responsible for the metal becoming ionized and being transferred into the bulk solution. However, the transport of the metal ions from the corrosion site is rather slow if there is no flow of the bulk solution over the corrosion site. The ions become trapped in the area of the pit and affect the chemistry of the solution. The ion concentration can reach a point where the solubility constant (K_{sp}) of the ion in the solution is exceeded. At this point the metal ion can undergo hydrolysis following the reaction:

$$M^{m+} + H_2O \Rightarrow M(OH)^{(m-1)+} + H^+ \qquad (2)$$

The OH^- ions combine with metal ions from the surface and thereby lower the pH at that location. For most metals and alloys, passive films formed at intermediate pH values are not stable at lower pH values. Therefore as the pH drops, dissolution of the passive film leaves the metal unprotected. This thereby accelerates the propagation of the pit. While the overall surface of the material may be experiencing rather low corrosion rates, the pit

could be corroding at rates orders of magnitude higher. Figure 7 schematically shows the above described pit initiation process.

Physical flaws in the passive film also play an important role in pit initiation. These flaws are attributed to several factors. If nucleation and lateral growth are responsible for the growth of the three dimensional passive film, then impingement of the growing regions may result in defects due to crystallographic mismatch. Also, a dimensional change can lead to a flaw in passive films (16). Both of these conditions could be possible in iron aluminides, and it is important due to the fact that without initiation there can be no pit propagation.

Pit propagation can be interrupted however. Once a pit is initiated, it may or may not freely propagate into the base material. In some conditions, the surface within the pit may actually repassivate before significant penetration occurs. This can be caused either by the kinetics of pit propagation being too slow or by the formation of another stable oxide on the surface of the pit. If the propagation rate is too slow, the ions within it may diffuse or be transported by some other method away from the pit site. This would bring the solution in the pit back to equilibrium with the bulk solution in which it is assumed that the material had a thermodynamically stable passive film. Therefore, the material would repassivate by forming a new passive film if there is not too much debris or non-viable passive film oxide in the pit to block its growth. Also, there is the possibility with some elements, such as tungsten for instance, to form more stable oxides as the pH

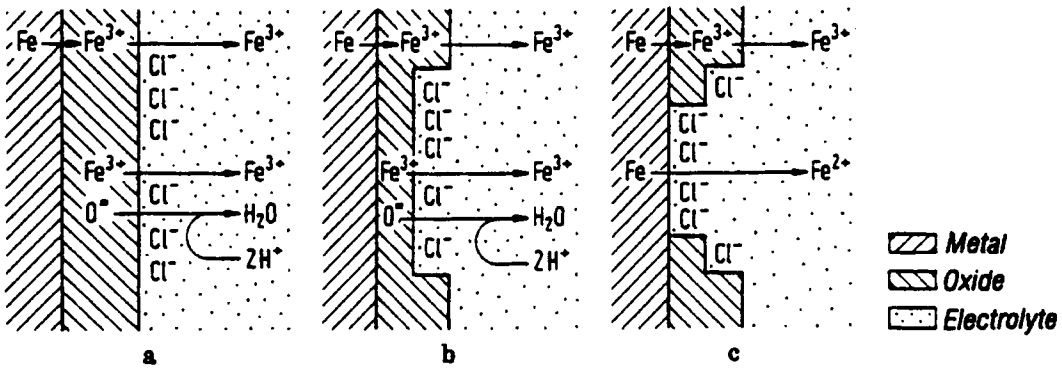

Figure 7: Initiation process for the local perforation of the passive oxide on iron in Cl^- containing solution of intermediate pH (17).

decreases. This oxide can then adhere to the surface of the pit if there is not too much debris to hinder passive film growth.

The repassivation or protection potential, E_p, of an alloy can be determined by performing cyclic anodic polarization tests, which will be discussed later. It is highly desirable for the alloy to have a protection potential which is higher than the free corrosion potential, E_{corr}, so that repassivation can occur. This would tend to indicate that even though the alloy is susceptible to localized pitting type corrosion, it will be able to repassivate and stop pit propagation at E_{corr}.

It also is known that molybdenum has a strong influence in increasing the pitting potential of many iron based alloys (16). Therefore, it was desired to see if it could have the same effect in iron aluminide alloys. This was investigated in the synthesis and testing of FAL-Mo which is very similar in composition and structure to FA-129 with the major exception of the addition of 1 atomic percent Mo.

2.3. Stress-Corrosion Cracking

Stress-Corrosion Cracking (SCC) is the term applied to the failure in engineering materials that occurs by often slow, environmentally induced crack propagation. The crack propagation is a result of the combined and synergistic interaction of corrosion reactions and mechanical stressing (18). The synergy is important to the mechanism of stress-corrosion cracking because neither corrosion nor mechanical stressing is influential enough on its own to cause failure. Despite this, stresses to cause stress-corrosion

cracking are small, usually below the macroscopic yield stress, and tensile in nature. These stresses can come from external loading or from residual stresses (18).

Stress-corrosion cracking is alloy/environment specific; that is, it is often the result of a specific chemical specie in the environment. Generally, stress-corrosion cracking is observed in alloy/environment combinations where there is passive film formation on the metal surface. As a result of this, stress-corrosion cracking is of greatest concern in corrosion-resistant alloys that are exposed to aggressive aqueous environments (18). Stress-corrosion cracking leads to macroscopically brittle fracture where there is nearly no contraction at the fracture surface. Crack propagation proceeds by a sometimes alternating action of electrochemical and mechanical processes. The electrochemical process consists of an anodic dissolution of metal at the bottom of the crack which is being driven by strongly adsorbing anions which prevent repassivation. The adsorption reduces the surface energy at the crack tip making continued cracking easier (3). A model of the electrochemical process is shown in Figure 8. The mechanical process produces an array of dislocations ahead of the advancing crack, resulting in an embrittlement of the material.

Stress-corrosion cracks can initiate at pits that form during exposure to the service environment or during cleaning operations, such as pickling. This makes it especially important to understand the formation of pits on the surface of iron aluminides, for these pits can be initiation sites for stress-corrosion cracking. However, the transition between pitting and cracking depends on the parameters that control stress-corrosion cracking:

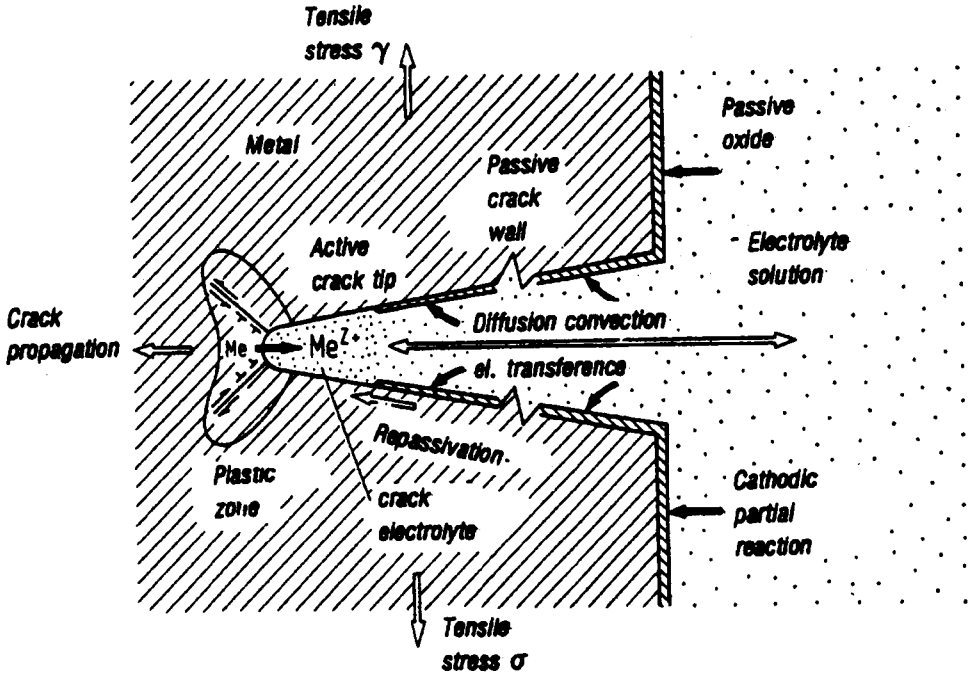

Figure 8: Electrochemical model for stress corrosion cracking of a passive alloy by anodic metal dissolution at the zone of plastic deformation in advance of the crack tip (17).

electrochemistry at the base of the pit, the pit geometry, chemistry of the material, and the stress or strain rate at the base of the pit. There are examples of pre-existing pits that did not initiate cracks. This indicates that perhaps electrochemistry of the pit is more important than the local stress or strain rate. A preexisting pit may not develop the same local electrochemistry as one grown during the service life (18).

2.4. Hydrogen Embrittlement

The presence of hydrogen in many materials leads to a reduction of the tensile ductility and causes a premature failure under static loading which is dependent upon stress and time. It is usually characterized by little plastic deformation in what is normally a ductile material and the mode of fracture is usually cleavage, quasi-cleavage, or intergranular fracture. The effect of hydrogen is most pronounced when the strain rate is low and increases with decreasing strain rate. It also is prevalent at room temperature. This suggests that the effect of hydrogen is time dependent. Also, moderately high temperatures will cause hydrogen to diffuse out of the material. The two structures most susceptible to hydrogen embrittlement are body-centered cubic and hexagonal close-packed.

Two mechanisms of hydrogen evolution are shown in Figure 9. In each case the breakdown of molecular hydrogen follows these reactions:

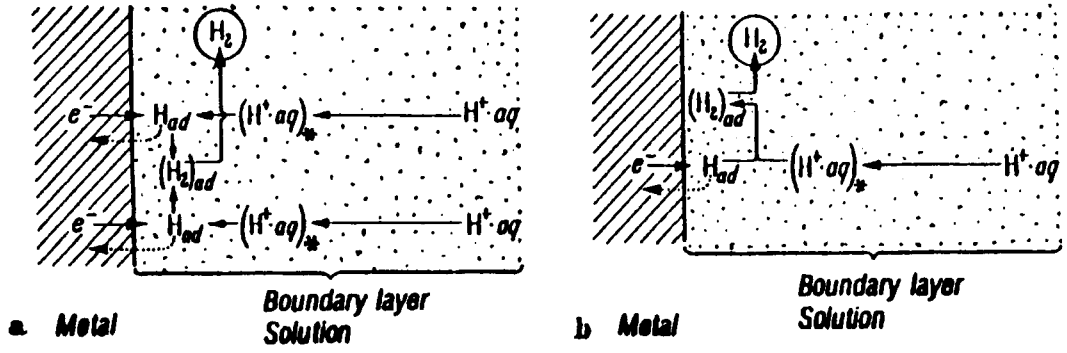

Figure 9: Reaction schematic for cathodic hydrogen evolution: (a) according to Volmer-Tafel, (b) according to Volmer-Heyrovsky mechanism (3).

$$H^+ \Rightarrow (H^+)\bullet \quad (3)$$

$$\left(H^+\right)\bullet + e^- \Rightarrow H_{ad} \quad (4)$$

$$H_{ad} + H_{ad} \Rightarrow \left(H_2\right)_{ad} \quad (5)$$

$$H_{ad} + \left(H^+\right)\bullet + e^- \Rightarrow \left(H_2\right)_{ad} \quad (6)$$

Equation 3 denotes the migration of the of H^+ from the bulk solution to the metal surface, denoted by $(H^+)\bullet$ in the above equations. The specie then combines with an electron at the surface. In Equation 4, the hydrogen ion from the bulk solution in Equation 3 acquires an electron from the metal which eliminates its charge. It can then either adhere to the surface of the material and be absorbed into it or follow Equations 5 or 6. It is the absorption process of atomic hydrogen that leads to hydrogen embrittlement. However, in Equation 5 atomic hydrogen on the surface of the material can combine with another and form molecular hydrogen. The molecular hydrogen will form a bubble on the surface and not be absorbed into the material. Equation 6 shows another way that atomic hydrogen can form a hydrogen molecule on the surface. Molecular hydrogen is not responsible for hydrogen embrittlement since it is not absorbed into the material (17), (19).

Hydrogen embrittlement occurs in the aforementioned process through hydrogen ion reduction in an acid solution. However, it can also occur through corrosion processes in a neutral solution as illustrated in Figure 10. In this figure, hydrogen production is occurring during crack propagation as a variation on the pitting model. This production of hydrogen is also very similar to the process that occurs to produce hydrogen

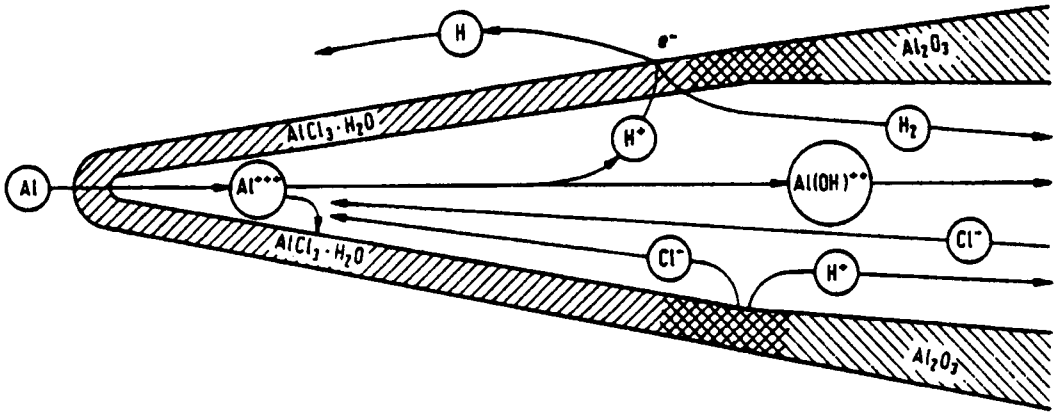

Figure 10: Crack propagation through local "anodic" hydrogen embrittlement (17).

embrittlement in iron aluminides. The process is governed by the following anodic and cathodic reactions, respectively:

$$2Al + 3H_2O \Rightarrow Al_2O_3 + 6H^+ + 6e^- \quad (7)$$

$$6H^+ + 6e^- \Rightarrow 6H \quad (8)$$

These are the reactions that produce atomic hydrogen at the aluminum surface (10). Once the atomic hydrogen is produced it follows Equations 2-4 for either absorption or evolution as gas bubbles.

There are several theories as to why hydrogen causes embrittlement in metals. The pressure theory claims that the embrittlement is caused by the diffusion of hydrogen into the metal and it accumulates in voids or other internal surfaces in the alloy. The pressure will continue to increase until cracking occurs due to high hydrogen pressures (20).

There is also an absorption and decohesion model where embrittlement does not arise from hydrogen being uniformly distributed in solid solution. The interstitial element can usually be found in regions of high triaxial stress ahead of the crack. Hydrogen adsorption at the crack tip generates the localization of plastic flow and microvoid coalescence. The cohesive strength in that region is thereby reduced, and a crack is nucleated when the level of hydrogen reaches a critical value (21), (22).

Figure 11 shows the relationship between the growth rates of stress-corrosion cracks in aluminum alloy 7075 exposed to air as a function of the relative humidity (23). It can be seen that the crack propagation rate is directly proportional to the water content in the air. The reactions in Equations 7 and 8 are known to happen, which leaves hydrogen

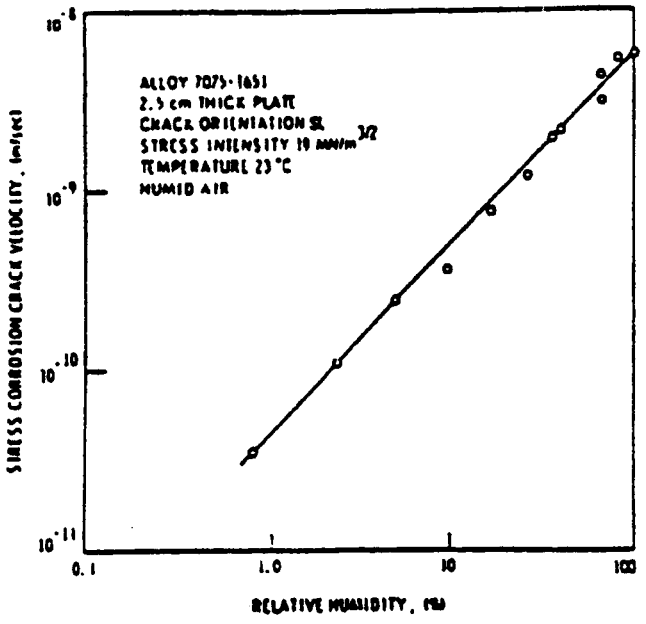

Figure 11: Effect of humidity on the stress independent subcritical crack growth rate in a high-strength aluminum alloy exposed to humid air (3).

embrittlement as the only explanation of environmentally induced subcritical crack growth (SCC) in aluminum alloys. This is a plausible explanation for iron aluminide systems, which is supported by the results of a decrease or an absence of hydrogen embrittlement in oxygen containing atmospheres. In these atmospheres, the oxygen, by an anodic reaction with aluminum, can form Al_2O_3 as well as combine with atomic hydrogen to form H_2O as long as the vapor content is not already too high or the oxygen content too low.

2.5. Cyclic Anodic Polarization Test

The cyclic anodic polarization test is used to determine relative susceptibility to localized corrosion (either pitting or crevice corrosion). An indication of the relative susceptibility to initiation of pitting corrosion in this test is the breakdown potential forpitting corrosion, $E_{b,pit}$, which is the potential at which the anodic current density begins to rapidly increase and continues to increase until reaching a predetermined reversing current density, i_r. These and other features of a cyclic anodic polarization curve are shown in Figure 12. The higher $E_{b,pit}$ the more resistant the material is to pitting corrosion in that test environment. However, the results of this test are not intended to correlate in a quantitative manner with the rate of propagation that might be observed in a service environment when localized corrosion occurs. A polarization test is an artificial test of the material's behavior in an environment because of the severity of the potentials that are applied as well as the large current densities (24). It is most useful for

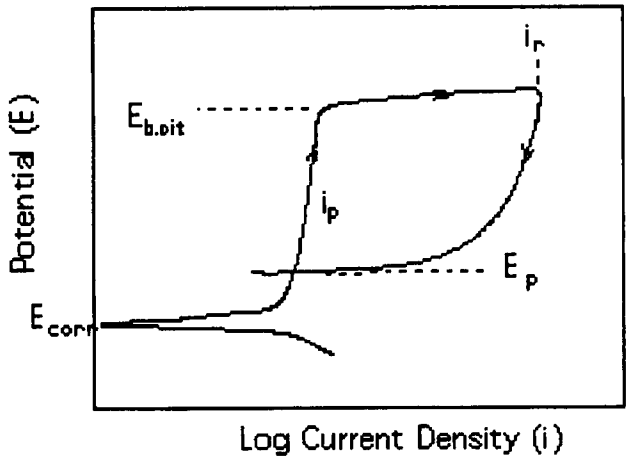

Figure 12: Schematic cyclic polarization curve.

determining whether an alloy will suffer from localized corrosion and for quickly comparing one alloy to another alloy in an environment to see which is better suited.

Once a pit is initiated, localized corrosion can continue for some time longer while the down scan or hysteresis loop is completed. It is at the point at which the hysteresis returns to the passive current density , i_p, on the polarization curve that the protection potential, E_p, is located. The passive current density is marked by the portion of the anodic curve which is nearly vertical. In this region, the current is approximately constant for increasing applied potentials. It is a measure of the passive corrosion rate on the surface of the sample. A corrosion current density of from 10^{-1} to 10^{1} $\mu A/cm^2$ is an acceptable range for the passive current density. Anything greater denotes that the passive film is too unstable and is not adequately slowing uniform corrosion.

The protection potential denotes the material's ability to resist pit propagation once a pit has initiated. If E_p is below E_{corr}, then a pit-like defect will freely propagate at E_{corr}. If E_p is above E_{corr}, then the material is protected from pitting in that if a pit should initiate, then the pit will repassivate in that electrolyte. However E_p is not a material characteristic, but a function of scan rate. The hysteresis loop is an indication of localized corrosion. If there is no hysteresis then the material's increase in current density was caused by a uniform thermodynamic breakdown of the passive film, which produces uniform corrosion, not localized corrosion.

2.6. U-Bend Test

The U-bend test specimen can be used for any metal alloy that has sufficient ductility to be formed into a "U" shape without mechanically cracking. A U-bend specimen is most easily made from strip or sheet but can also be made from strips machined from plate, bar, castings, or weldments.

The U-bend test is one of the most severe tests for smooth (as opposed to notched or pre-cracked) stress-corrosion samples because it usually contains large amounts of elastic and plastic strain. Yet the stress conditions are not usually known and a wide range of stresses can be present in a specimen. This makes U-bend specimens unsuitable for studying the effect of different applied stresses on stress-corrosion cracking. The U-bend specimen is advantageous because it is simple and economical to make and use. It also is most useful for detecting large differences between stress-corrosion cracking resistance of (1) different metals in the same environment, (2) one metal in different metallurgical conditions in the same environment, or (3) one metal in several environments.

Typical U-bend geometries are shown in Figure 13 (25). There are several geometries that are applicable and for a more detailed comparison the total strain (ε) on the outside surface of the bend can be closely approximated by the equation:

$$\varepsilon = \frac{T}{2R} \text{ when } T << R \qquad (9)$$

where T = specimen thickness and R = radius of bend curvature (25).

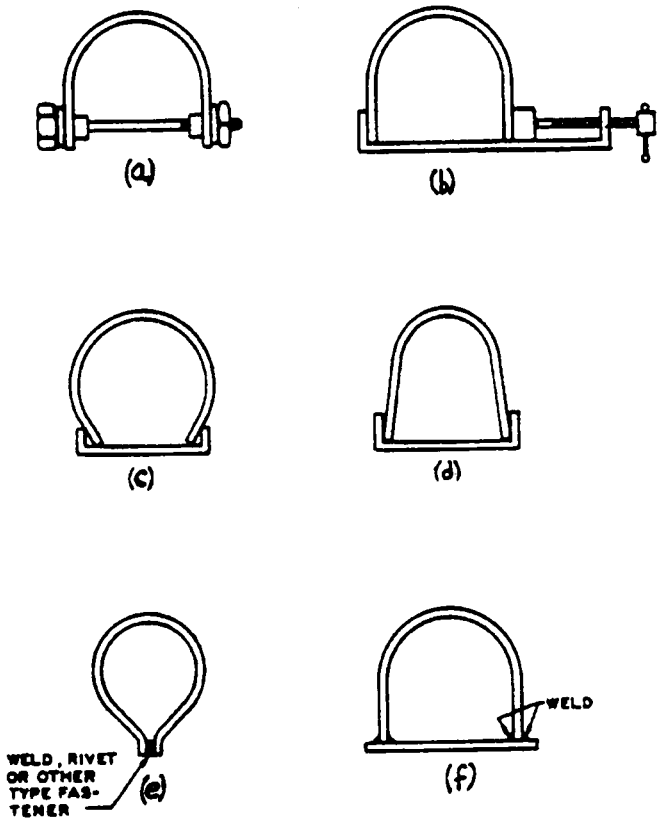

Figure 13: Typical stressed U-bends (25).

2.7. Slow Strain-Rate Testing

The slow strain-rate test (SSRT) involves a tensile machine which pulls a smooth sample that is exposed to a corrosive solution at a low crosshead velocity. It was developed initially as a rapid laboratory method for assessing the tendency for metals and environments to promote stress corrosion cracking (26). It is used to screen alloys for new process equipment applications, to identify alloys that should not experience stress corrosion cracking during service, and to verify that existing equipment will not undergo stress corrosion cracking when it placed in new service conditions (27).

Typical strain rates for the slow strain-rate test is on the order of 10^{-6}/s which is about 4 orders of magnitude slower than a standard tensile test. Cracking susceptibility is indicated by a decrease in mechanical properties over those observed in an inert environment. A major advantage of slow strain-rate testing over constant load or constant deflection testing is that the test usually involves shorter times, more data, and sometimes a much more conclusive result. Slow strain-rate testing also is less costly than fracture mechanics crack propagation tests because the specimen geometry and test procedures are simpler (27).

When a constant strain rate is applied to a tensile specimen, film rupture is insured to occur and slip step emergence is induced artificially. The severity of cracking can be controlled to a certain extent since rate of slip-step emergence is controlled by the strain rate (28).

Under static loading conditions, the onset of localized corrosion in the form of pitting gives rise to an increase in the stress in the metal under the pits, leading to slip step emergence and creating the active condition of corrosion. During slow strain-rate testing, the active condition of the metal is always maintained as the dynamic strain creates new metal surface by slip-step emergence. Strain rate is the important experimental parameter in the slow strain-rate test.

Although the slow strain-rate test method is effective for producing cracking in systems where it is difficult to produce cracking in static systems, a specific range of strain rates must be employed before stress corrosion cracking can occur. If a strain is chosen that is too high, even if initiation of stress corrosion cracking occurs, the cracks become blunted due to dynamic strain before any significant amount of localized corrosion can occur at the crack tip. Therefore, no stress corrosion cracking will be observed. In other words, the crack propagation proceeds more quickly than does the corrosion kinetics, so corrosion cannot make a significant contribution to embrittlement of the alloy. If the strain rate is too slow, the corrosion reaction will proceed to such an extent that it will be obstructed by film formation and the active condition at the crack tip cannot be maintained (28). This is shown schematically in Figure 14.

Also shown in Figure 14 is the difference in dependency for hydrogen induced cracking on strain rate. This is caused by fact that hydrogen-induced cracking does not require a film-rupture event, but is brought about by occluded hydrogen in the alloy. During the corrosion reaction for hydrogen cracking, the cathodic half-cell reaction

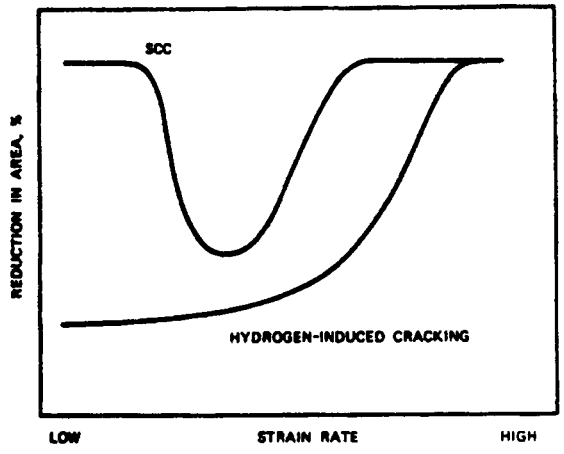

Figure 14: Schematic presentation of the effect of strain rate on SCC and hydrogen induced cracking (28).

produces hydrogen on the metal reaction surface. Some of this hydrogen is adsorbed by the alloy until it reaches the saturation limit. As the testing period is increased by decreasing the strain rate, the sample becomes more susceptible to hydrogen cracking. As the strain rates approach those of normal tensile tests, then the time for hydrogen production and adsorption is not available and hydrogen embrittlement will not be observed (28).

Since there is dynamic straining occurring, the passive film at the surface is being ruptured by the inability of the passive film to yield with the material. This local inability to maintain the passive film leads to three conditions that are conducive to high localized corrosion rates (32). First, in the absence of the passive film the anodic polarization curve is estimated by the extension of the active region of the curve from the active potential to the corrosion potential. A second possible condition is caused by the electrochemical difference between the new exposed metal surface area and the passive film. This difference can generate a small electrical current between the two opposing surfaces. The relatively small area of the exposed anodic metal surface compared to the large area of the surrounding passive film results in an unfavorable anode-to-cathode ratio. This causes a high local current density and induces high metal dissolution at the anode. The current generated by general corrosion in the passive state is subtracted from the total current to obtain the current created only by pit growth (29). The third condition is a consequence of the change in the composition of the electrolyte in the confined region of the localized attack.

While slow strain-rate testing is useful for detecting stress corrosion cracking, some discrepancies can arise in certain alloy-environment systems where cracking in known to occur. This could be due to incubation time effects, potential range effects, and strain rate effects. Most reported cases of the anomalous behavior with the slow strain-rate test can be attributed to inadequate control or measurement of strain rate or potential, which are the major controlling parameters for a specific material/environment combination (27).

Metallographic examination is essential to the interpretation of slow strain-rate results. It can provide both qualitative and quantitative descriptions of stress corrosion cracking severity in slow strain-rate tests. A qualitative description of stress corrosion cracking severity for carbon steel in CH_4-CO_2-CO aqueous solutions in slow strain-rate tests is shown in Figure 15. Cross sections through slow strain-rate specimens indicate a range of behavior from shallow pits or no corrosion, shown at the right of the figure, to severe general corrosion shown at the left. Between these extremes is the domain of stress corrosion cracking. The forms of corrosion/cracking shown toward the left of the figure are favored by increased corrosivity, higher concentration of CO_2 or O_2, lower concentrations of CO, and more positive anodic potentials (30).

Measurement of specimen ductility in the slow strain-rate test provides a convenient parameter of stress corrosion cracking severity. Reduction of area or elongation can be used. A comparison is made between ductility under conditions of interest and under conditions which do not promote stress corrosion cracking. Loss in ductility is attributed to stress corrosion cracking with more severe stress corrosion cracking corresponding to

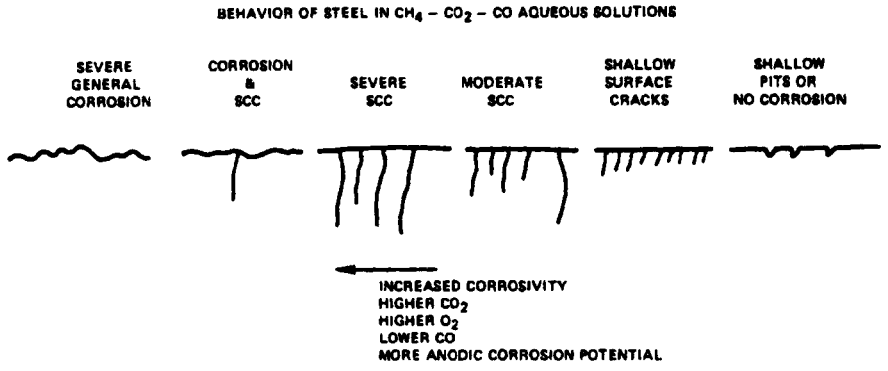

Figure 15: Range of corrosion behavior of carbon steel in CH_4-CO_2-CO aqueous solutions (30).

greater loss of ductility. However, in this instance, metallographic examination is imperative since other causes in loss of ductility exist besides stress corrosion cracking. One example is hydrogen embrittlement. Cathodic charging of hydrogen into steel in caustic solutions during slow strain-rate tests results in a severe loss of ductility but no SCC (30).

The slow strain-rate test has been found to be a conservative test. When stress corrosion cracking susceptibility is not found in the test, no stress corrosion cracking was predicted in service for the conditions tested. Conversely, when susceptibility is found in slow strain-rate tests, an alloy may be acceptable for an application, and no stress corrosion cracking failures may be experienced if the stresses are insufficient to sustain stress corrosion cracking. It still must be recognized that the particular metal/solution combination is susceptible to stress corrosion cracking and given sufficient stresses, failure can occur (30).

The occurrence of strains in service comparable to those imposed on a metal during slow strain-rate tests is not as rare as might be expected. Even though most designs do not anticipate appreciable plastic strains in service, strains on the order of creep rates are of interest and can result in stress corrosion cracking. Service failures have been observed in a variety of applications where the nominal stresses were well below the yield stress of the metal. Strains can result from the additive effects of operating loads, pressure fluctuations, thermal stresses, and residual stresses during normal operation, start-up or shut-down (30).

III. Experimental Procedures

Cyclic anodic polarization tests were conducted in an electrochemical solution to evaluate the active/passive behavior as well as the relative stabilities of the passive films within the solution. These tests were performed to examine the relative differences between surface conditions. U-bend stress corrosion tests were carried out on the surface conditions tested during the polarization tests. The tests were conducted for 200-hours, or until fracture, to measure the effects of the electrochemical potential and constant stress on cracking behavior. Slow strain-rate corrosion tensile tests were conducted in the same electrochemical solution as the polarization tests and at different electrochemical potentials to observe the variations in ductilities and strength as a result of hydrogen embrittlement.

3.1. Materials

All of the iron aluminides were produced at Oak Ridge National Laboratory. Heats of 500 g were arc melted in water-cooled crucibles in a chamber backfilled with argon. Buttons were remelted six times for homogeneity. Following this the melts was drop cast into a copper mold to form 25 x 12 x 125 mm ingots. The ingots were then hot forged 50% at 1000°C, hot rolled 50% at 800°C, and warm rolled 70% at 650°C to a finish thickness of 0.75 mm. FA-84, FA-129, FAL-Mo, and FAPY were provided in sheet form for the polarization tests. FA-385 came in a cladded rod form for polarization testing. Slow strain-rate samples were punched out of sheet stock of FAL, FAL-Mo, and

FA-129 by Oak Ridge National Laboratory and then machined to final geometry at the University of Tennessee. Chemical compositions for all materials tested are shown in Table 1. Heat treatments for the tests were: (1) heat treating in air at 750°C for one hour to stress relieve the sheet as well as produce a reproducible oxide for testing, followed by an oil quench to preserve the B2 ordered structure, and (2) heat treating in air at 1000°C for 24 hours to generate an Al_2O_3 oxide surface followed by furnace cooling so as to promote oxide adherency to the iron aluminide surface. The 750°C heat treatment was performed on the sheet stock to create a high temperature oxide on the surfaces after they were cleaned of the as-processed thermomechanical surface. Polarization tests were run on the as processed and oxide surfaces to see if their corrosion properties were similar. This was necessary because the U-bend test could not utilize the as-processed surface.

Table 1: Chemical compositions of iron aluminides (atomic percent).

	Fe	Al	Cr	Mo	B	Zr	Nb	C	Y
FA-84	69.9	28.0	2.0	-	0.05	-	-	-	-
FA-129	66.3	28.0	5.0	-	-	-	0.5	0.2	-
FA-385	63.9	36.7	-	.2	-	0.05	-	0.11	-
FAL	66.9	28.0	5.0	-	-	0.1	-	-	-
FAL-Mo	65.9	28.0	5.0	1.0	0.04	0.08	-	-	-
FAPY	77.2	16.1	5.4	1.1	-	0.1	-	-	0.06

All strips had to be heat treated prior to bending so as to stress relieve them, otherwise they would fracture upon bending. This heat treatment on the as-processed surface would change it. The morphology and structure of the oxide could be changed in such a way that the behavior of the heat treated as-processed surface might not be the same as the as-processed surface. Therefore, the 750°C furnace oxide was desired for usage in testing because of its reproducibility as well as its ease of use. The Al_2O_3 oxide was produced to simulate the surface created during high temperature service. To differentiate between the different oxide surfaces, "as-processed" will refer to the surface in the thermomechanical, as-received condition, "750°C furnace oxide" will refer to the oxide formed at 750°C for one hour in air, and "1000°C furnace oxide" will refer to the oxide formed at 1000°C for 24 hours in air.

3.2. Cyclic Anodic Polarization Test

Sample preparation for polarization testing is very important because poor laboratory techniques can induce certain conditions that can manifest themselves in the test. A prefabricated sample holder was used in place of epoxy mounting since the prefabricated holder did not require grinding of the sample surface. Grinding to remove the excess epoxy would remove either the as-processed oxide or the furnace oxide.

Surface preparation for the different surface conditions varied. To prepare the furnace oxide surface, the samples were cut into the appropriate size and then ground to remove the as-processed surface. The surface was polished through 600 grit SiC. It was then

heat treated for one hour at 750°C and oil quenched to produce the furnace oxide. The mechanically cleaned surface was prepared by doing similar cutting and heat treating. Following the heat treatment, the sample was ground and polished through 600 grit. The chemically cleaned surface was produced in a similar fashion to the mechanically cleaned surface up until the step following heat treatment. At this point a pickling solution commonly used on stainless steels was employed to clean the surfaces. The solution and variations on it were (1) 10% HNO_3, 2% HF at 43°C for FAL-Mo, (2) 10% HNO_3, 2% HF at 25°C for FA-129, and (3) 10% HNO_3 at 43°C for FA-84, FAPY could not be chemically cleaned suitably for polarization testing. All samples were chemically cleaned until the oxide was removed by visual inspection. At this point the samples were given a passivation treatment of immersion in 10% HNO_3 at 43°C for one hour.

The prefabricated holder required that the sheet stock be cut into 2 x 2 cm square blanks for testing. The blanks were painted with epoxy (Amercoat 90, Ameron, Brea, CA) following appropriate surface preparation so as to cover the area where the prefabricated holder made contact with the blank. This interface is a suitable crevice corrosion initiation site which would interfere with the measurement of $E_{b,pit}$. A window was left on the sample of a known area so that the current density could be calculated.

Once a blank was placed in the holder, the holder was placed in a standard electrochemical corrosion cell. It was allowed to remain in solution while the open-circuit corrosion potential was monitored so as to determine when the corrosion potential had

stabilized. A stable corrosion potential was one that met the condition of ± 1 mV change per minute. If this step is not carried out, then the results obtained from the polarization test will be erroneous.

The cell contained a gas inlet, the sample as the working electrode, a platinum counter electrode, and a salt bridge for the calomel reference electrode. The electrodes were connected to an EG&G Model 273 potentiostat which applied a continuously varying potential to the working electrode, beginning from an initial potential approximately 35 mV less than E_{corr} and scanning upward at a scan rate of 600 mV/h until a reversing current density of 1000 $\mu A/cm^2$ was reached (31). At this point, the scan was reversed until it reached a potential that was predetermined so as to determine E_p. The potentiostat was interfaced with a computer which displayed the data as the test proceeded. The computer saved the data in a binary format which was converted to ASCII format at the same time that the potentials were converted from the saturated calomel reference electrode scale to the standard hydrogen electrode scale.

3.3. U-Bend Stress-Corrosion Cracking Test

The dimensions of the U-bend specimens are shown in Figure 16. The strips were cut from sheet stock received from Oak Ridge National Laboratory. The holes were then drilled into the strips with a carbide drill bit. Following the drilling, the strips were then ground in the longitudinal direction through 600 grit SiC. The strips were heat treated for

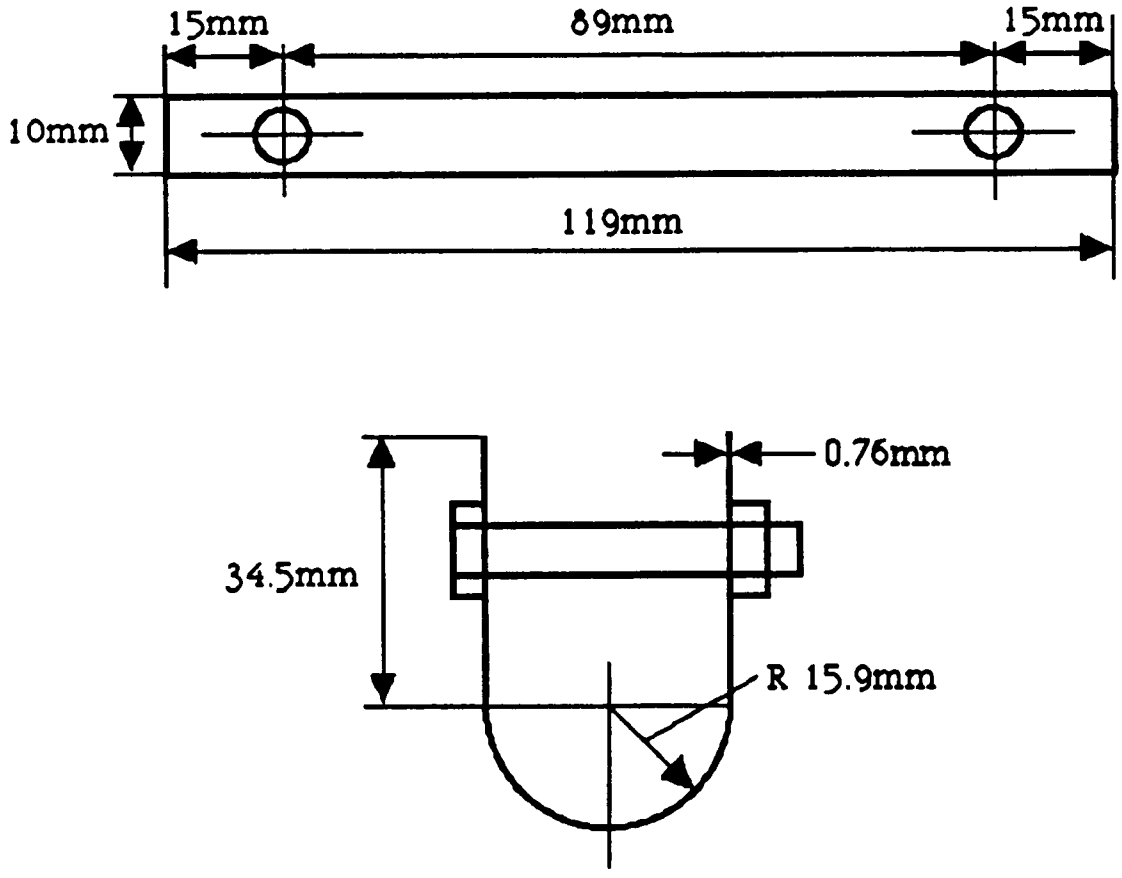

Figure 16: U-bend test specimen geometry (3).

one hour at 750°C, to place an oxide on the surfaces and stress relieve the rolled sheets, and then oil quenched. The oil quenching was used to protect the strips from moisture during cooling as well as to insure that the B2 superlattice was preserved. Half of the samples were cleaned of the furnace oxide, again by grinding through 600 grit SiC, to form the mechanically cleaned surface condition. A titanium wire was then spot welded to the strips to establish electrical contact for either potential measurement or application of potential. The strips were then painted with epoxy from the ends inward for 1.5 cm on each end. This covered the spot weld so as to eliminate galvanic corrosion effects. The strips were bent in a jig shown schematically in Figure 17. Once bent in the jig, a polyvinyl chloride bolt was placed through the holes without lowering the jig. The bolt was tightened until the sides of the strip were parallel.

The U-bend specimens were immersed in a mild acid chloride solution [pH=4 (H_2SO_4), 200 ppm Cl^-] for 200-hours. During the 200-hour test, the specimens were either at the free corrosion potential or potentiostatically held at -1500 mV SHE. The manner of stressing guaranteed that the outer fiber stress was beyond the yield stress. This was determined by preliminary bends that were made to determine if a U-bend specimen could be made without fracturing the strip. Once a strip was bent, the jig was lowered without placing the bolt in the holes. The strips held a visible amount of bend afterwards which proved that there was permanent plastic deformation of the strips. Also, the distance between the parallel arms of the U-bend specimen was measured before

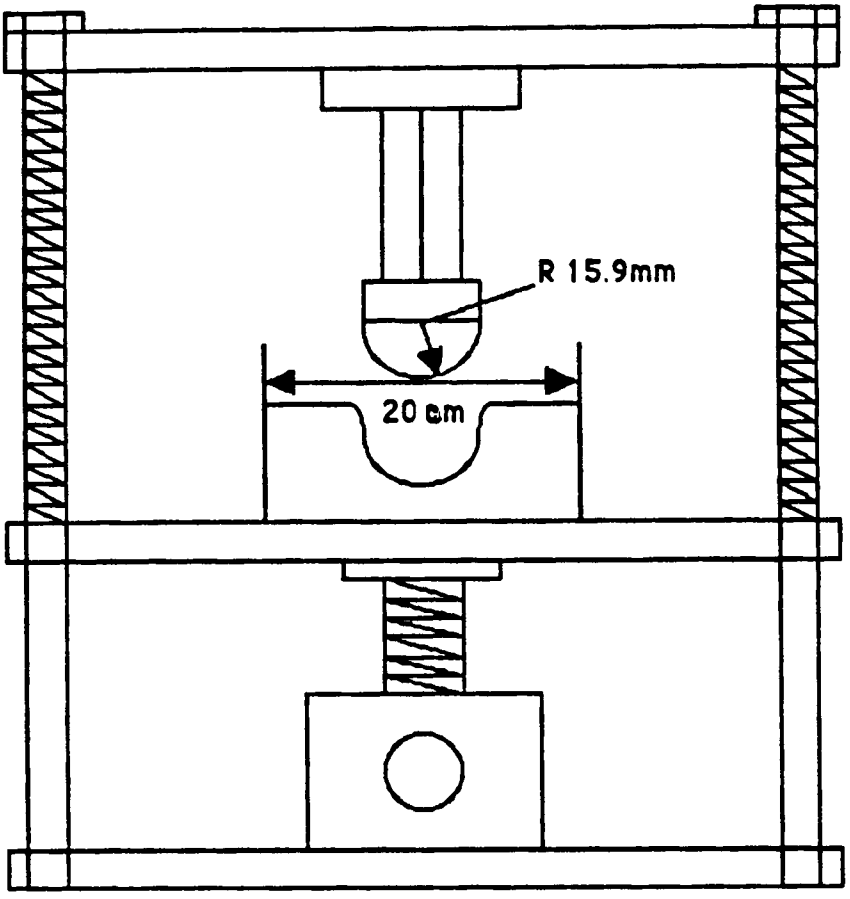

Figure 17: Schematic of U-bend test jig (3).

and after the test to confirm that the polyvinyl chloride bolt had not undergone creep during the 200-hour test.

3.4. Slow Strain-Rate Tensile Testing

The slow strain-rate test samples were punched out of sheet stock at the Oak Ridge National Laboratory. The punched samples then were machined to the geometry shown in Figure 18. The change in geometry was in the gage section which had to be narrowed to prevent problems that arose in earlier slow strain-rate tests where the samples broke unacceptably close to the grip section. The next step involved drilling the holes in the grip sections. Punching the holes in previous test specimens proved to introduce too much residual stress and caused the sample to break within the grip section. The samples were then polished through 600 grit SiC to remove the as-processed thermomechanical surface oxide. All samples were then heat treated in an alumina crucible for 24 hours at 1000°C in air and then furnace cooled. The alumina crucible was used to avoid concerns about possible contamination of the Al_2O_3 oxide on the iron aluminide surface that could be introduced from other crucibles. Furnace cooling was employed to promote adherency of the oxide to the iron aluminide surface. A titanium wire was spot welded to the samples to make electrical contact for either measuring the corrosion potential or for applying a cathodic potential.

The slow strain-rate corrosion tests were conducted in the load frame shown schematically in Figure 19. It contained a test cell which consisted or a glass vessel with a

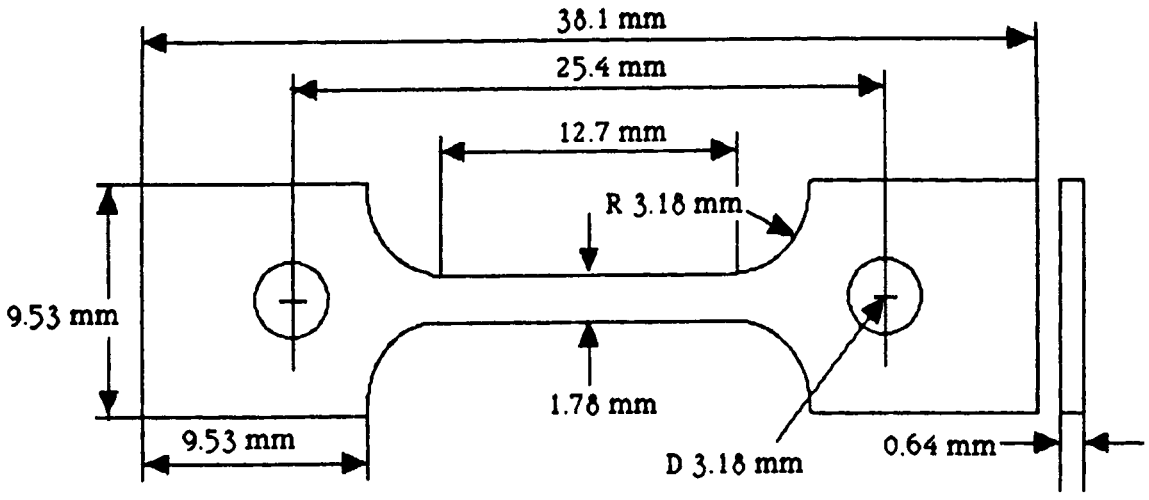

Figure 18: Slow strain-rate test specimen geometry (3).

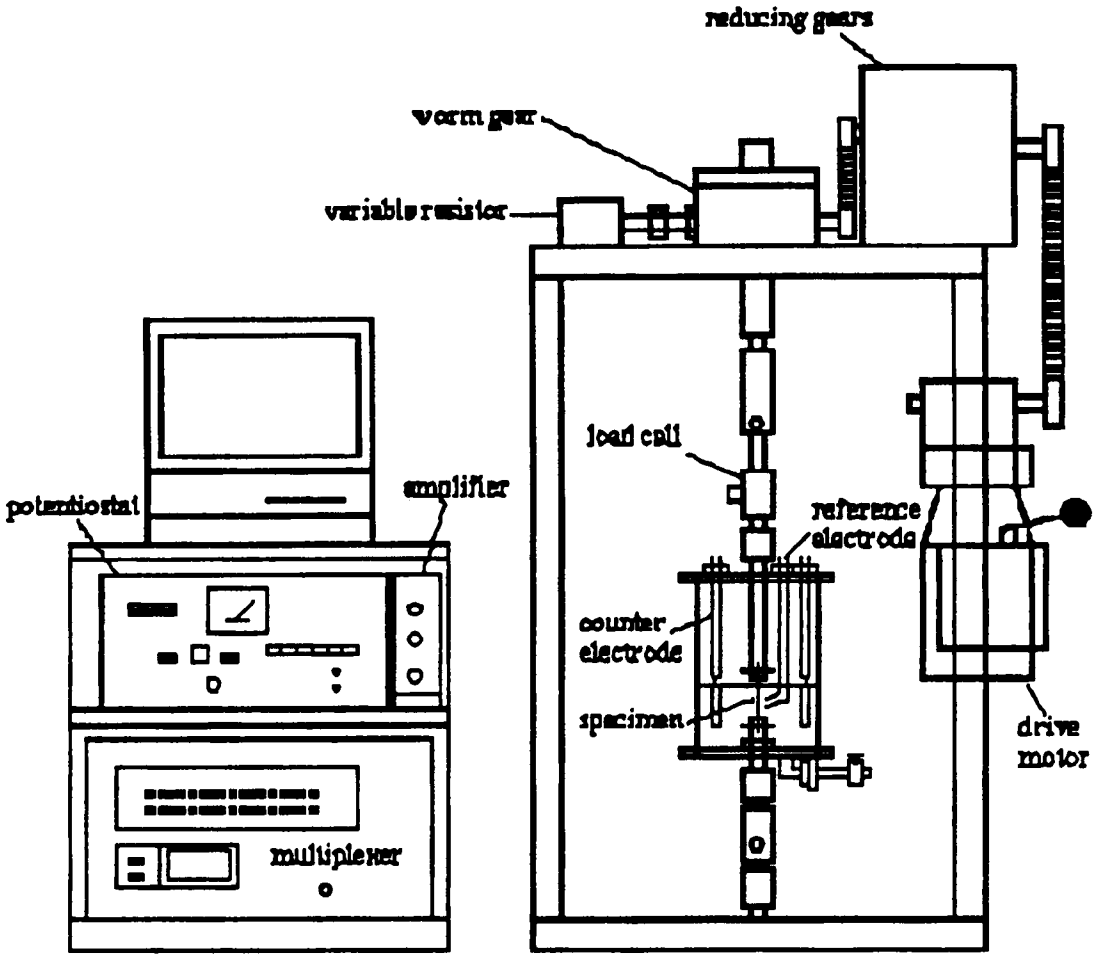

Figure 19: Schematic diagram of slow strain-rate facility (3).

polyvinyl chloride top and bottom. The top section contained access ports for the titanium wire welded to the sample, a platinum counter electrode, and the salt bridge for use with the saturated calomel reference electrode. The top and bottom sections of polyvinyl chloride had compression fittings that allowed them to be tightened to the glass cell, independent of the load frame, which provided a suitable seal for the electrolyte in the test cell. The sample was secured to the load frame by means of iron aluminide pins that were coated with epoxy. The epoxy was used to eliminate galvanic effects, and iron aluminide was chosen as the pin material in case the epoxy cracked, thereby further minimizing galvanic effects. The tensile force applied to the specimen was monitored with a Sensotec, Model 41/571-07, 500 pound load cell. The cell received its excitation voltage from a Sensotec Model 450D power-supply/amplifier. The output of the amplifier was monitored by a multiplexer which in turn was monitored by a Samsung S330 personal computer. During any one test, the load, cross-head displacement, and either the specimen corrosion potential or the cathodic current density were monitored. The two sample surface conditions employed during the tests were either mechanically cleaned or 1000°C furnace oxide. The two potentials used were either -1500 mV SHE or the open circuit corrosion potential.

IV. Results and Discussion

The effect that surface condition has on the aqueous corrosion and environmentally assisted cracking characteristics of iron aluminides are presented and discussed in this section. The aqueous corrosion properties of the iron aluminides were evaluated in a mild acid chloride [pH=4, 200 ppm Cl^-] electrolyte which is designed to simulate aggressive atmospheric exposure. Cyclic anodic polarization tests were used to analyze the passivation behavior and susceptibility to localized corrosion of the iron aluminides under static (no load) conditions. The stress-corrosion behavior was evaluated by means of U-bend tests as well as slow strain-rate tests. The solution used was the same mild acid chloride electrolyte used for the polarization tests.

4.1 As-Processed and 750°C Furnace Oxides Versus Cleaned Surfaces

4.1.1 Polarization Results

4.1.1.1. FA-84

Polarization results for the as-processed, mechanically cleaned, and chemically cleaned surfaces of FA-84 are shown in Figure 20. The as-processed condition, relative to the mechanically cleaned and chemically cleaned conditions, produced a lower pitting potential ($E_{b,pit}$), and a higher corrosion potential (E_{corr}). The lower $E_{b,pit}$ value and the lower difference between E_{corr} and $E_{b,pit}$ for the as-processed (high-temperature oxide) surface condition both indicated reduced resistance to pitting corrosion. The decreased i_p

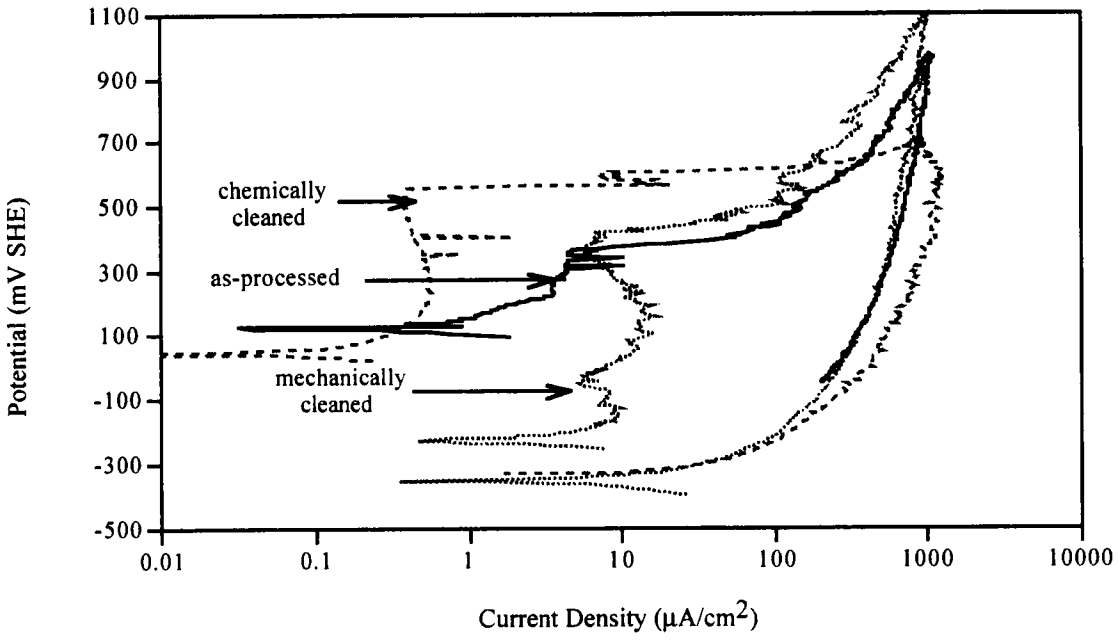

Figure 20: Comparison of as-processed, mechanically cleaned, and chemically cleaned surfaces of FA-84.

for the chemically cleaned surface suggests that the chemical cleaning process enhanced the properties of the passive film, most likely by thickening it.

Figure 21 shows the comparison of the as-processed and 750°C furnace oxide surfaces. It can be seen that neither surface exhibited much pitting resistance. Both surfaces had passive films that produced progressively increasing current densities until a final breakdown that led to pit propagation. Overall, the polarization behavior of the 750°C furnace oxide surface was much more similar to that of the as-processed surface than to the mechanically cleaned or chemically cleaned surfaces. This observation is significant because the 750°C furnace oxide surface had to be used in the U-bend tests (in place of the as-processed surface) for comparison with the mechanically cleaned surface.

4.1.1.2 FA-129

Figure 22 shows the comparison of as-processed, chemically cleaned and mechanically cleaned surfaces of FA-129. The as-processed surface condition performed poorly with respect to both the mechanically cleaned and chemically cleaned surface conditions. The as-processed surface condition showed almost no tendency for passivation. For the as-processed surface, the pitting potential was significantly lower, and the corrosion potential higher, than for the other two conditions which involved removal of the high-temperature oxide. The lower $E_{b,pit}$ value and the lower difference between the values of $E_{b,pit}$ and E_{corr} for the as-processed surface condition both indicated reduced resistance to pitting corrosion. The chemically cleaned surface did not perform as well as the mechanically cleaned surface in that the passive current density did not stabilize before

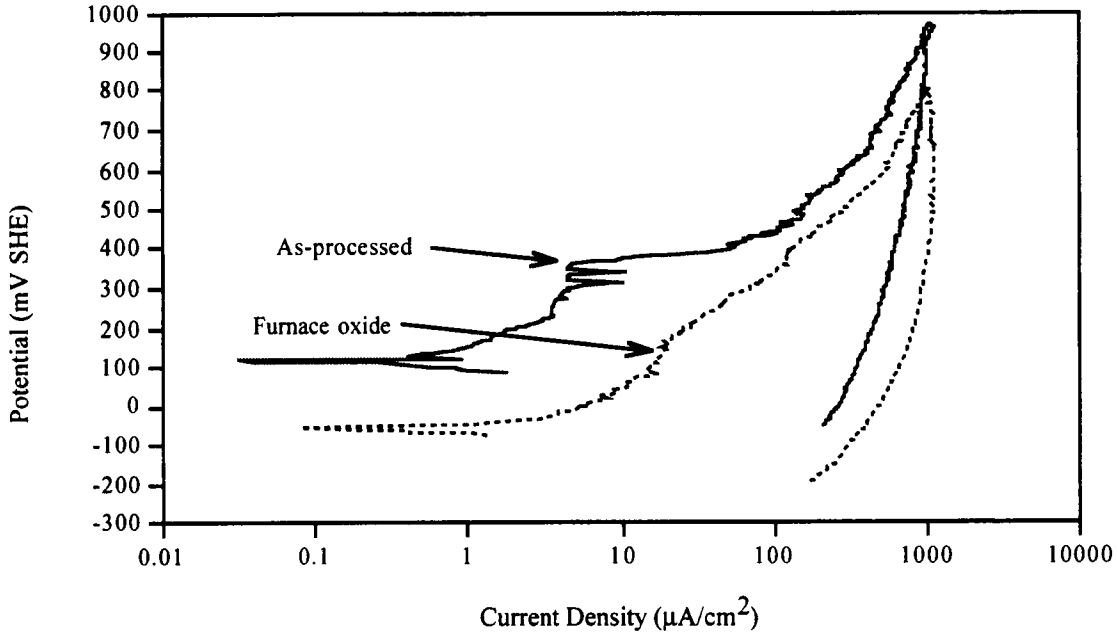

Figure 21: Comparison of as-processed and 750°C furnace oxide surfaces of FA-84.

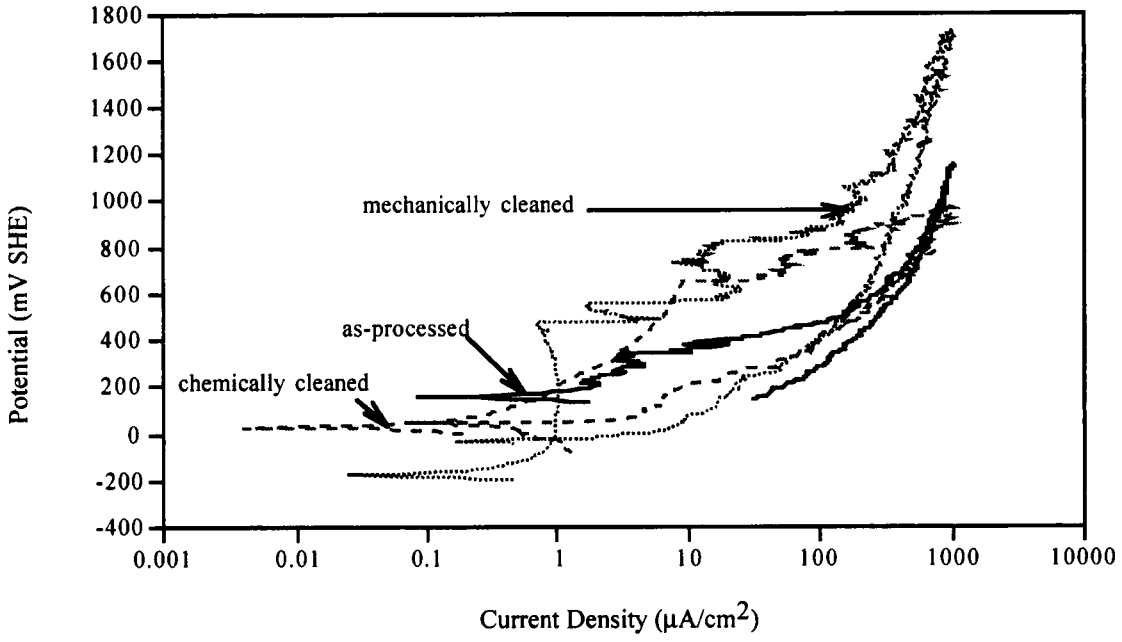

Figure 22: Comparison of as-processed, mechanically cleaned, and chemically cleaned surfaces of FA-129.

reaching $E_{b,pit}$. Even though the chemically cleaned surface had a higher breakdown potential, the difference between E_{corr} and $E_{b,pit}$ was greater for the mechanically cleaned surface than for the chemically cleaned surface. This thereby demonstrates that the best surface condition with respect to resistance to localized corrosion is the mechanically cleaned surface.

Figure 23 shows the polarization curves for the as-processed and 750°C furnace oxide surfaces of FA-129. It can be seen that the two surfaces had approximately the same $E_{b,pit}$, and generally low resistance to localized corrosion.

4.1.1.3 FAL-Mo

Figure 24 shows the comparison of the as-processed, chemically cleaned, and mechanically cleaned surfaces of FAL-Mo. It can be seen that the as-processed surface had a lower $E_{b,pit}$ than did both the chemically and mechanically cleaned surfaces. The as-processed surface also had a more unstable i_p than did the two cleaned surfaces. The difference between E_{corr} and $E_{b,pit}$ was the least for the as-processed surface and greatest for the mechanically cleaned surface. This suggests that the mechanically cleaned surface had the most resistance to localized corrosion. The chemically cleaned surface had a lower i_p than did the mechanically cleaned surface. The lower i_p indicated that there was either a thickening of the passive film or possibly a Cr enrichment of the passive film caused by the chemical cleaning process.

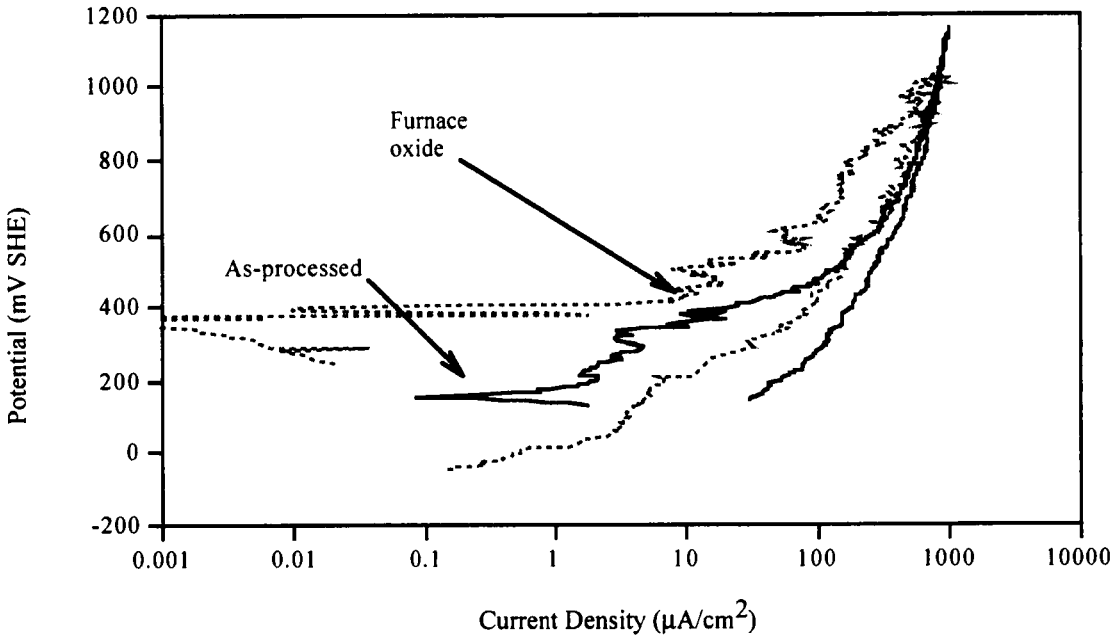

Figure 23: Comparison of as-processed and 750°C furnace oxide surfaces of FA-129.

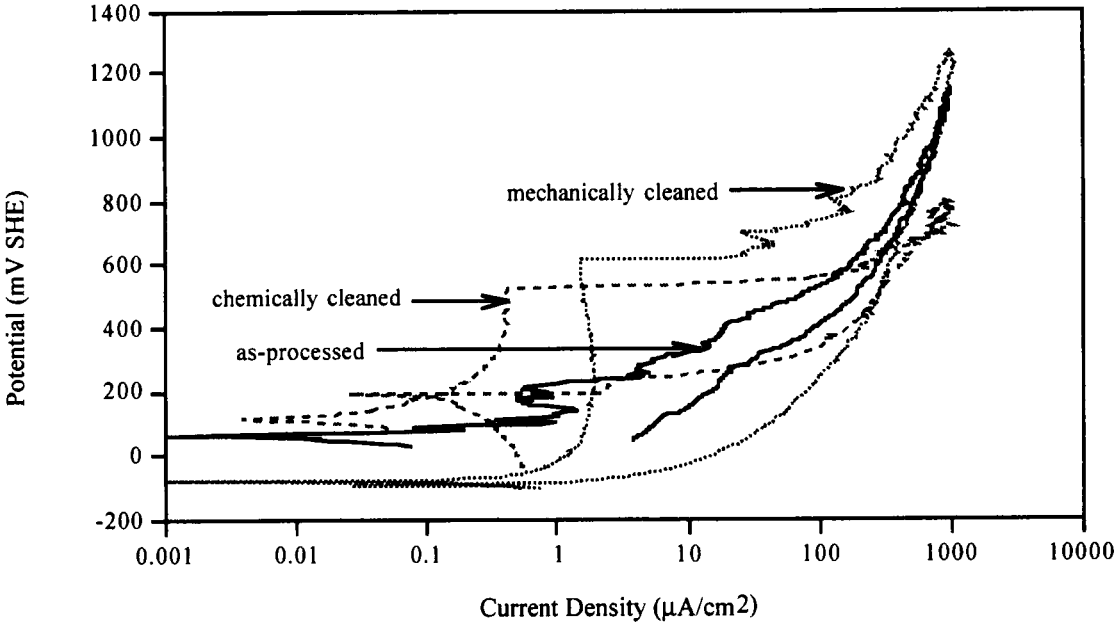

Figure 24: Comparison of as-processed, mechanically cleaned, and chemically cleaned surfaces of FAL-Mo.

Figure 25 shows the polarization curves for the as-processed and 750°C furnace oxide surfaces of FAL-Mo. It is seen that within experimental scatter, the two curves are nearly identical.

4.1.1.4. FAPY

Figure 26 shows the comparison of the cyclic anodic polarization behaviors of the as-processed, chemically cleaned and mechanically cleaned surfaces of the disordered alloy, FAPY. The chemically cleaned surface that was produced was covered with pockmarks which is not an acceptable surface for service, but the surface was tested with respect to cyclic anodic polarization. The as-processed surface performed poorly in comparison to the mechanically cleaned and chemically cleaned surfaces. The as-processed surface produced a much lower $E_{b,pit}$ with little indication of a passive current density, i_p, and a much higher E_{corr} value. The mechanically cleaned surface outperformed the chemically cleaned surface in certain respects as well. The mechanically cleaned surface had a significantly lower E_{corr} and only a slightly lower $E_{b,pit}$. Both surface conditions had a moderately strong tendency to repassivate. The chemically cleaned surface had a lower passive current density than did the mechanically cleaned surface but showed a little more instability as it approached $E_{b,pit}$.

Figure 27 shows the anodic polarization results for the as-processed and 750°C furnace oxide surfaces of FAPY. The behavior of the two surfaces was similar but differed in terms of potential ranges. The as-processed surface existed at higher potentials than did the furnace oxide surface. The differences in the polarization behavior could be

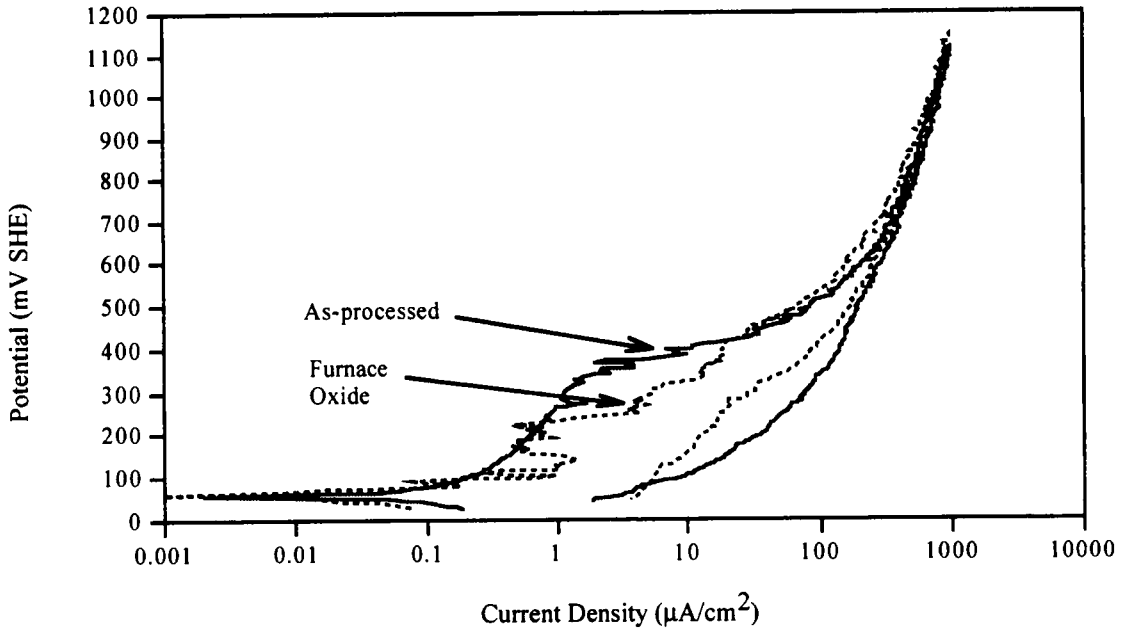

Figure 25: Comparison of as-processed and 750°C furnace oxide surfaces of FAL-Mo.

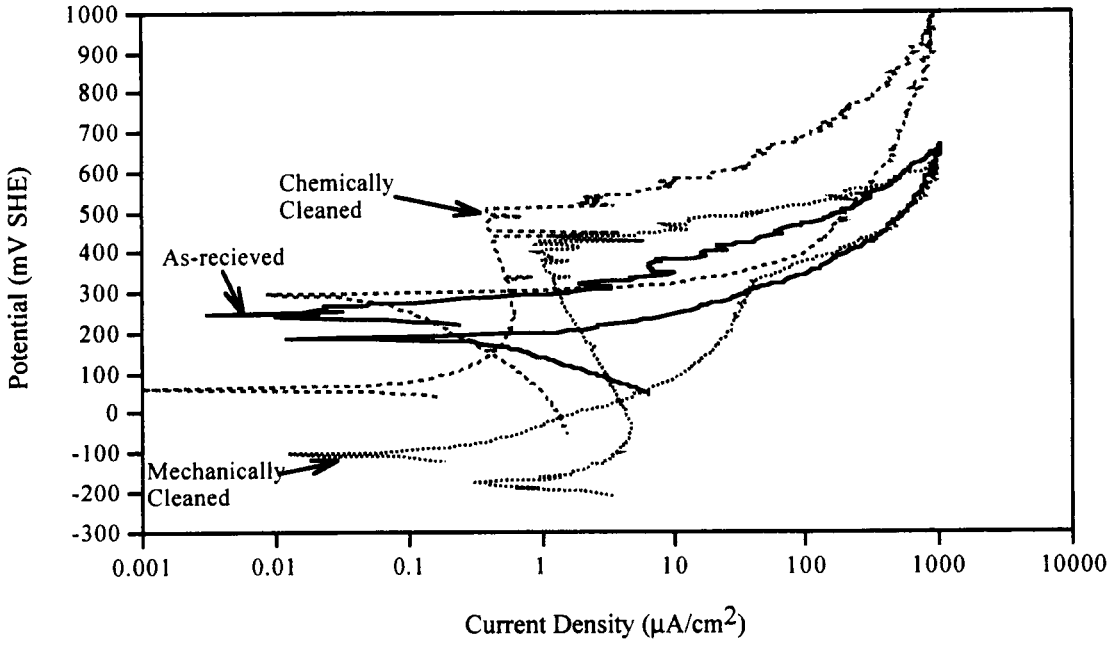

Figure 26: Comparison of as-processed, mechanically cleaned, and chemically cleaned surfaces of FAPY.

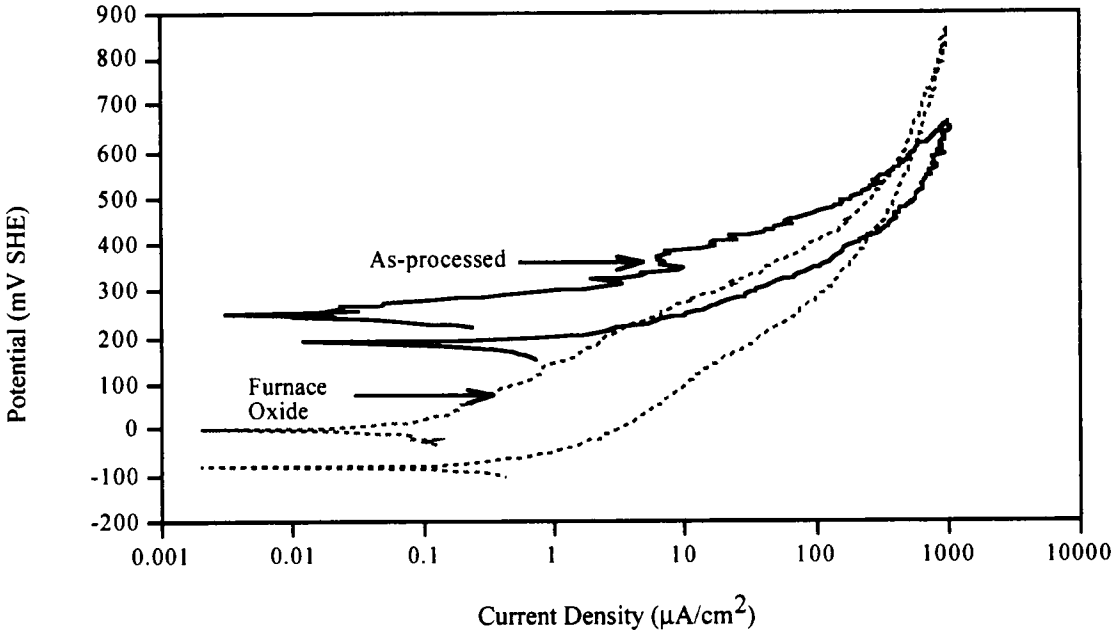

Figure 27: Comparison of as-processed and 750°C furnace oxide surfaces of FAPY.

related to the non-uniformity of the as-processed oxide surface compared to that of the furnace oxide surface. The hot working processes used on the as-processed surface created a very uneven oxide. On the other hand, the furnace oxide was mechanically polished through a 600 grit SiC finish and then heat treated to create the oxide. The surface of the furnace oxide was visually much smoother than was the surface of the as-processed oxide surface.

4.1.1.5. FA-385

Results for the FeAl based alloy FA-385 are shown in Figure 28. The two surface conditions examined were the mechanically cleaned surface and the 750°C furnace oxide surface. The heat-treated high-temperature-oxide surface condition produced a much lower $E_{b,pit}$, a much lower i_p, and a higher E_{corr} value than the mechanically cleaned surface condition. The lower $E_{b,pit}$ value and the lower difference between E_{corr} and $E_{b,pit}$ for the high-temperature-oxide surface condition both indicated reduced resistance to pitting corrosion.

4.1.2 Embrittlement (U-Bend) Results

The fracture results for all the U-bend tests are summarized in Table 2. The Table shows that no U-bend specimen fractured at E_{corr}. There were fractures only at the hydrogen charging potential of -1500 mV SHE and only for the samples that were in the mechanically cleaned condition. This indicates that the 750°C furnace oxide surface provides some protection from hydrogen penetration into the base material.

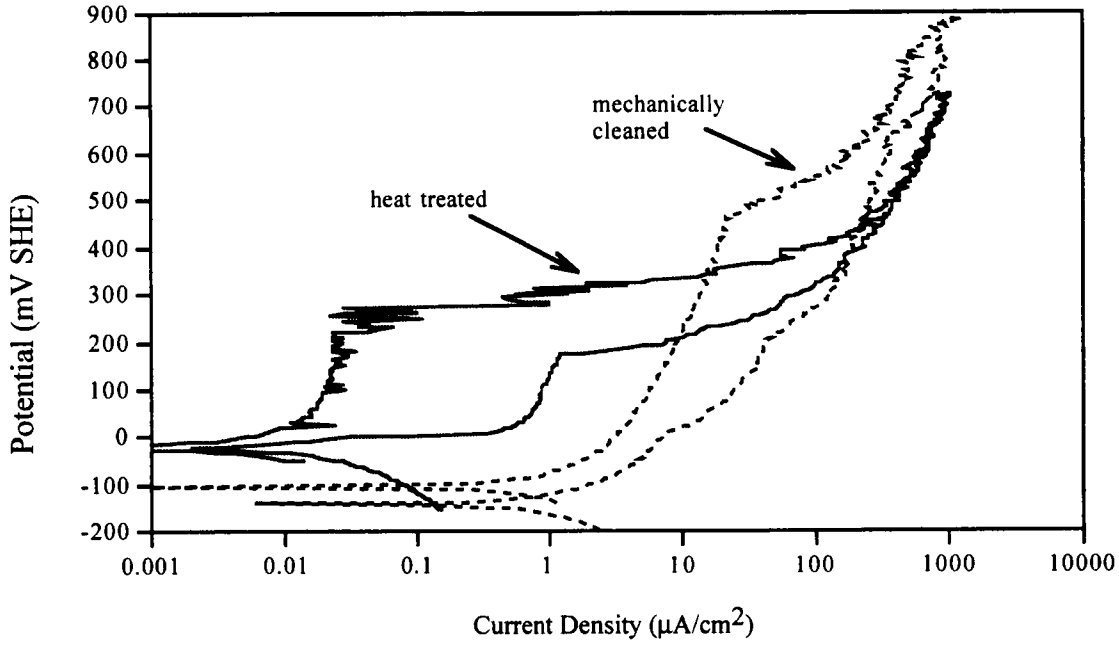

Figure 28: Comparison of mechanically cleaned and 750°C furnace oxide surfaces of FA-385.

Table 2: Summary of results of U-bend tests.

	E_{corr}		-1500 mV SHE	
Alloy	Mechanically Cleaned	750°C Furnace Oxide	Mechanically Cleaned	750°C Furnace Oxide
FA-84	No Cracking No Cracking	No Cracking No Cracking	Cracked (≈190 hr.) No Cracking	No Cracking No Cracking
FA-129	No Cracking No Cracking	No Cracking No Cracking	Cracked (≈23 hr.) No Cracking	No Cracking No Cracking
FAL-Mo	No Cracking No Cracking	No Cracking No Cracking	Cracked (≈190 hr.) No Cracking	No Cracking No Cracking
FAPY	No Cracking No Cracking	No Cracking No Cracking	No Cracking No Cracking	No Cracking No Cracking

4.1.2.1. FA-84

The corrosion potentials of FA-84 for the 200-hour U-bend tests are shown in Figure 29. The behavior of the alloy was as expected with respect to the initial corrosion potentials relative to surface conditions as indicated by the polarization results. Both samples showed progressive corrosion on the surfaces as well as corrosion products in the solution. However, neither sample broke during the 200-hour exposure.

The cathodic current densities for the 200-hour tests at -1500 mV SHE for the FA-84 U-bend specimens are shown in Figure 30. It can be seen that the oxide did not act to hinder the production of hydrogen at the oxide/solution interface. It did, however, act as a barrier to hydrogen penetration since the 750°C furnace oxide samples did not crack. One of the two mechanically cleaned samples did undergo cracking. These results illustrate that the furnace oxide reduced the hydrogen-embrittlement effect.

4.1.2.2. FA-129

The measured corrosion potentials for the 200-hour immersion tests of the FA-129 U-bend specimens are shown in Figure 31. It can be seen that the potential for the 750°C furnace oxide surface was higher initially than for the mechanically cleaned surface. This was consistent with results obtained from the polarization tests. During the 200-hour immersion, corrosion occurred visually on the furnace oxide surface but to a much smaller degree than on the FA-84 oxide sample. However, neither surface condition produced cracking in the U-bend samples.

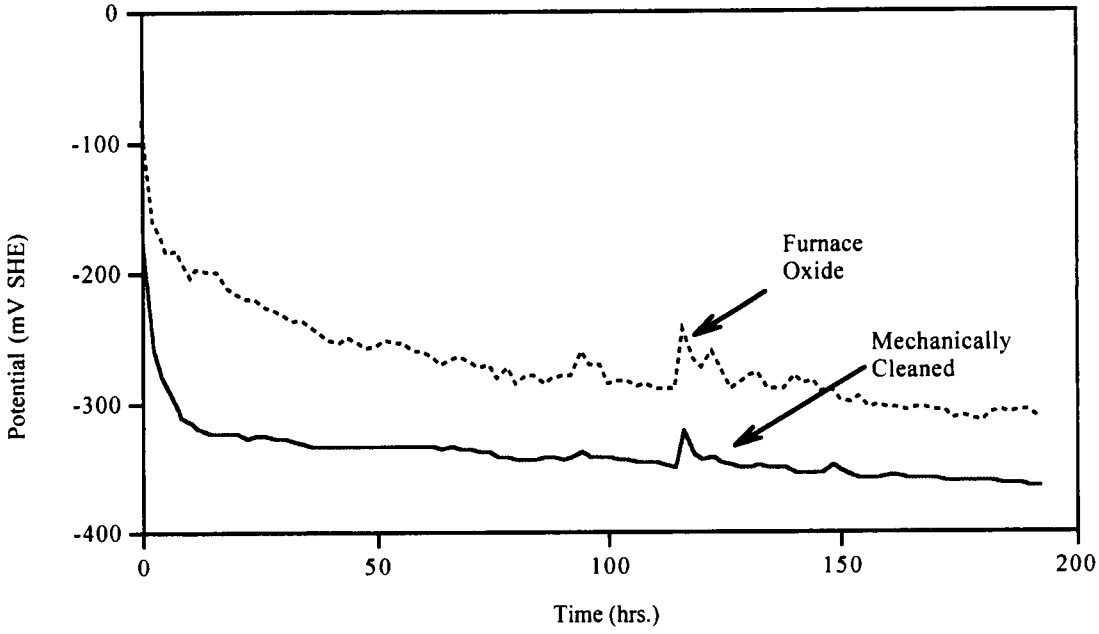

Figure 29: Free corrosion potentials for FA-84 during 200-hour U-bend tests.

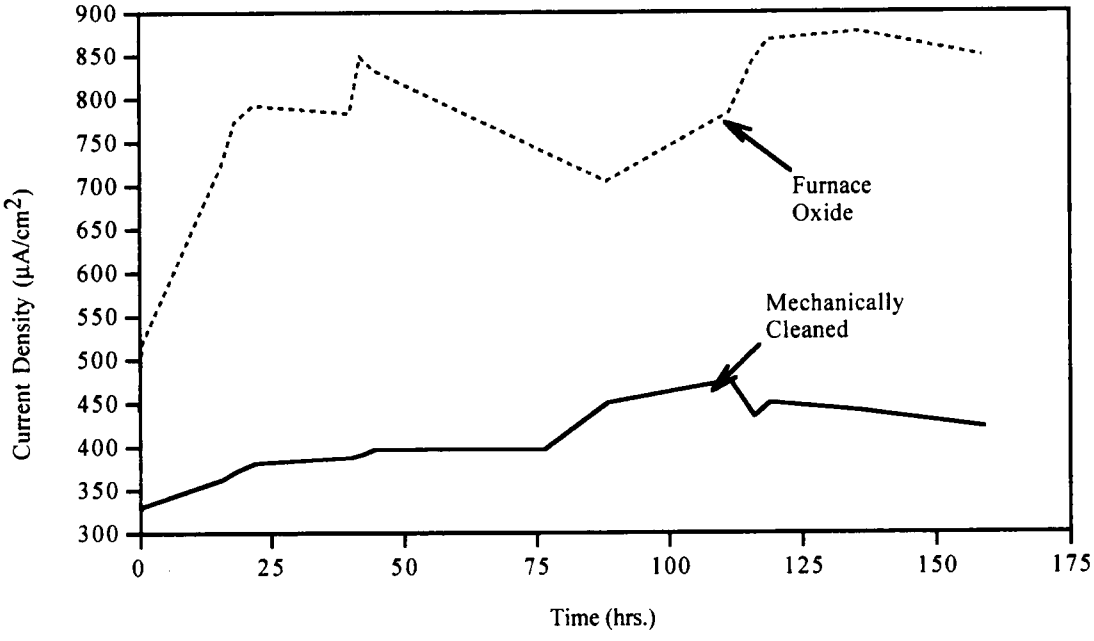

Figure 30: Cathodic current densities for 200-hour U-bend tests at -1500 mV SHE for FA-84 specimens.

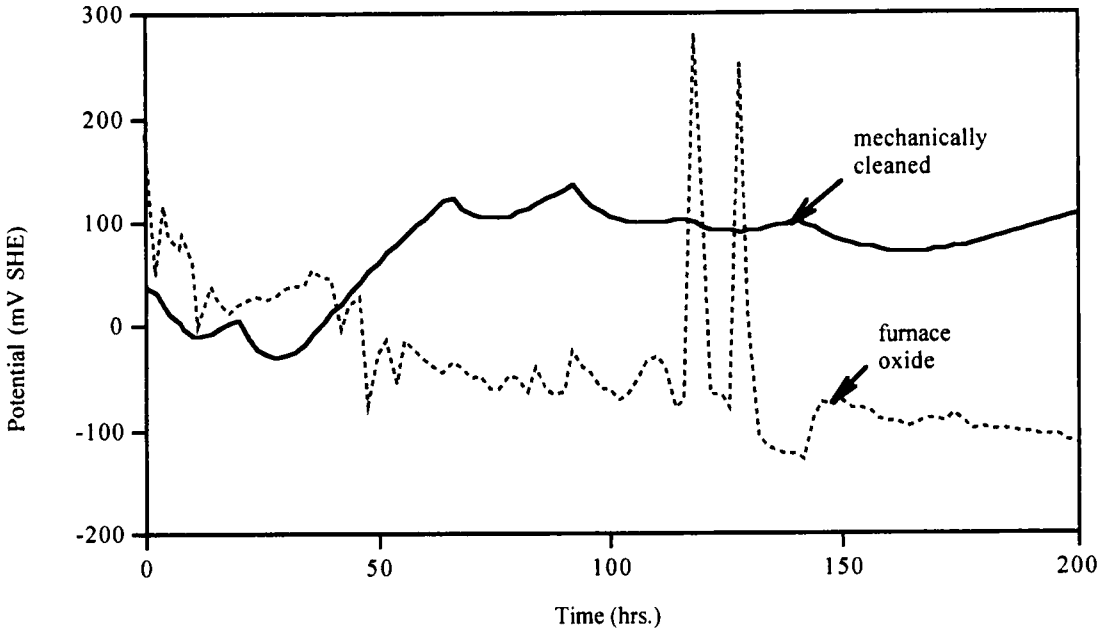

Figure 31: Free corrosion potentials for FA-129 during 200-hour U-bend tests.

Figure 32 shows the cathodic current densities measured during the 200-hour U-bend tests at -1500 mV SHE for FA-129. It can be seen that the cathodic current density for the mechanically cleaned surface was higher than that for the 750°C furnace oxide surface. It was the mechanically cleaned surface that fractured in this test. In this case, not only did the oxide hinder hydrogen production, but also served to protect the base material from hydrogen penetration.

4.1.2.3. FAL-Mo

Figure 33 shows the free corrosion potentials for the FAL-Mo U-bend samples during the 200 hour immersion tests. It can be seen that the free corrosion potential for the 750°C furnace oxide surface was higher than for the mechanically cleaned surface. Unlike the tests for FA-84 and FA-129 though, neither sample of FAL-Mo showed any visible signs of corrosion. Both samples came out of the test uncracked and virtually unchanged from their condition prior to the test.

Figure 34 shows the cathodic current densities for the FAL-Mo U-bend specimens at -1500 mV SHE during the 200-hour immersion tests. It can be seen that the cathodic current density was higher for the mechanically cleaned surface than for the 750°C furnace oxide surface for most of the test. The current density was also more constant throughout the test for the mechanically cleaned sample. This could denote more surface stability in the mechanically cleaned condition. However, the mechanically cleaned.

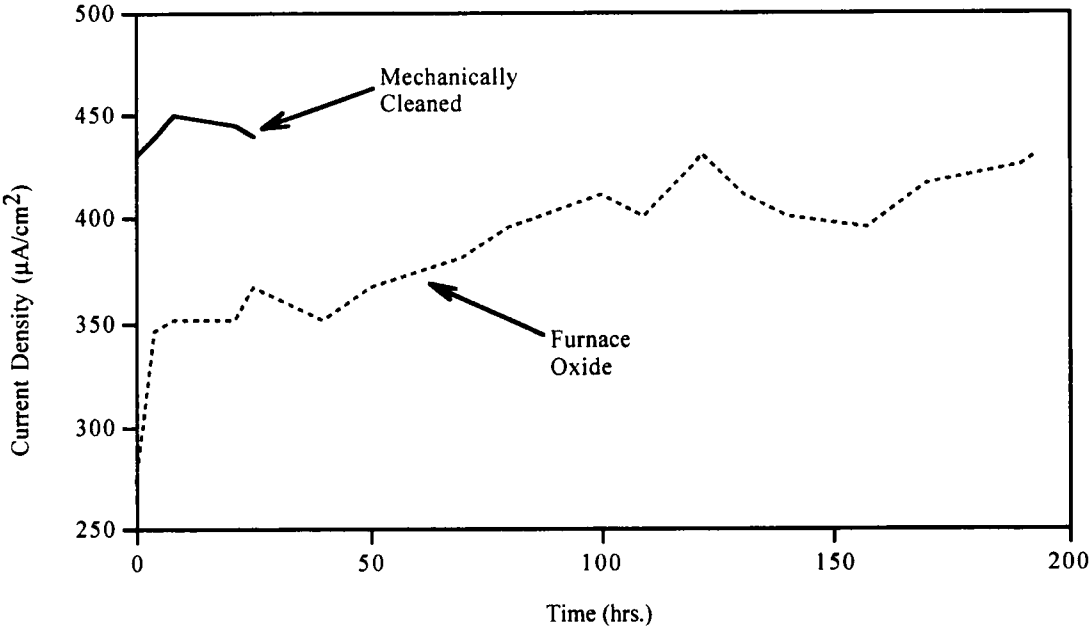

Figure 32: Cathodic current densities for 200-hour U-bend tests at -1500 mV SHE for FA-129 specimens.

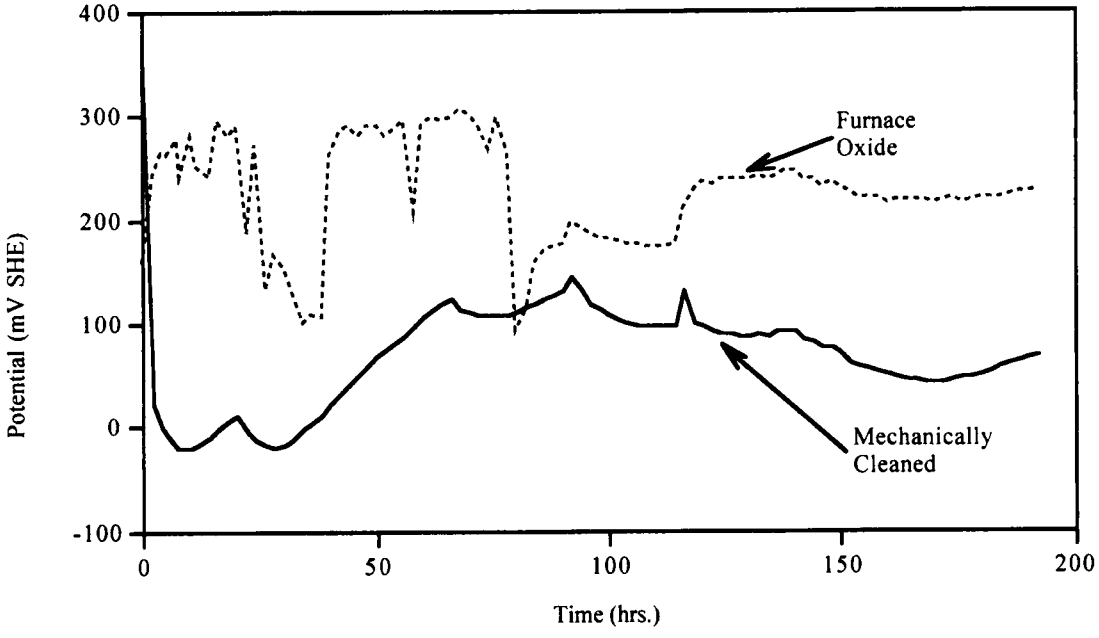

Figure 33: Free corrosion potentials for FAL-Mo during 200-hour U-bend tests.

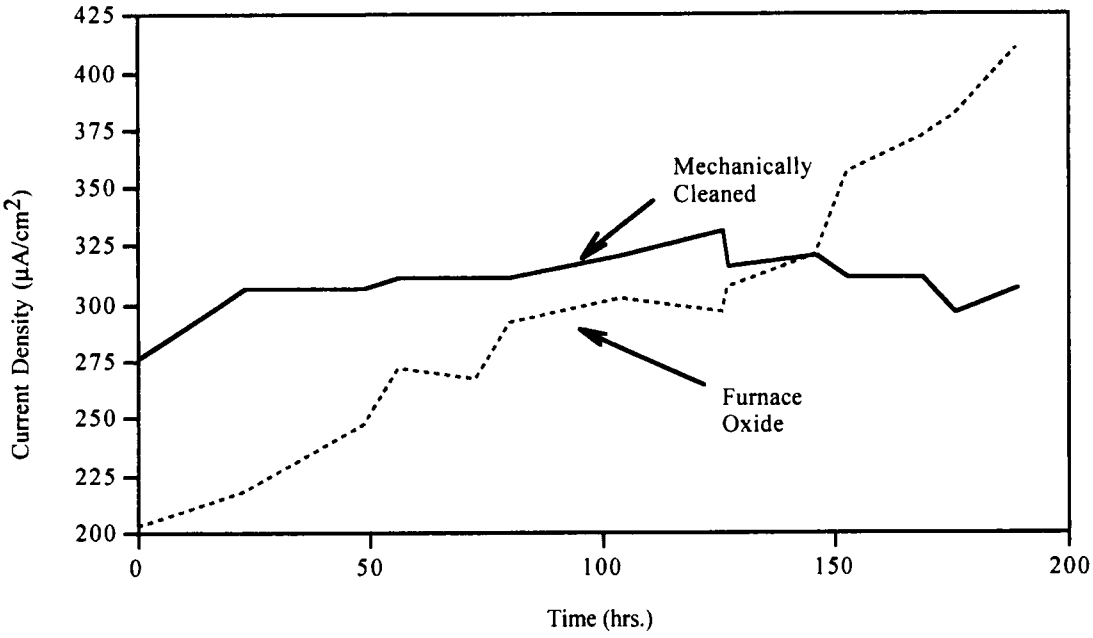

Figure 34: Cathodic current densities for 200-hour U-bend tests at -1500 mV SHE for FAL-Mo specimens.

specimen was the one that that underwent cracking. These results imply that the oxide surface decreased hydrogen production as well as retarding hydrogen penetration into the metal substrate.

4.1.2.4. FAPY

Figure 35 shows the free corrosion potentials of the FAPY U-bend specimens during the 200-hour immersion tests. The free corrosion potential for the 750°C furnace oxide surface was higher than for the mechanically cleaned surface, which is consistent with the polarization tests of FAPY. Even though the peaks in both curves might suggest that the samples were pitting during the test, inspection of Figure 35 indicates that any pits that initiate on the mechanically cleaned surface should repassivate before significant propagation. Neither specimen cracked during the 200-hour immersion test.

The cathodic current densities for the U-bend specimens of FAPY at -1500 mV SHE are shown in Figure 36. The current density for the mechanically cleaned surface was initially higher but over time the current density for the 750°C furnace oxide surface rose above that of the mechanically cleaned surface. None of the FAPY samples fractured during the U-bend tests at the hydrogen charging potential.

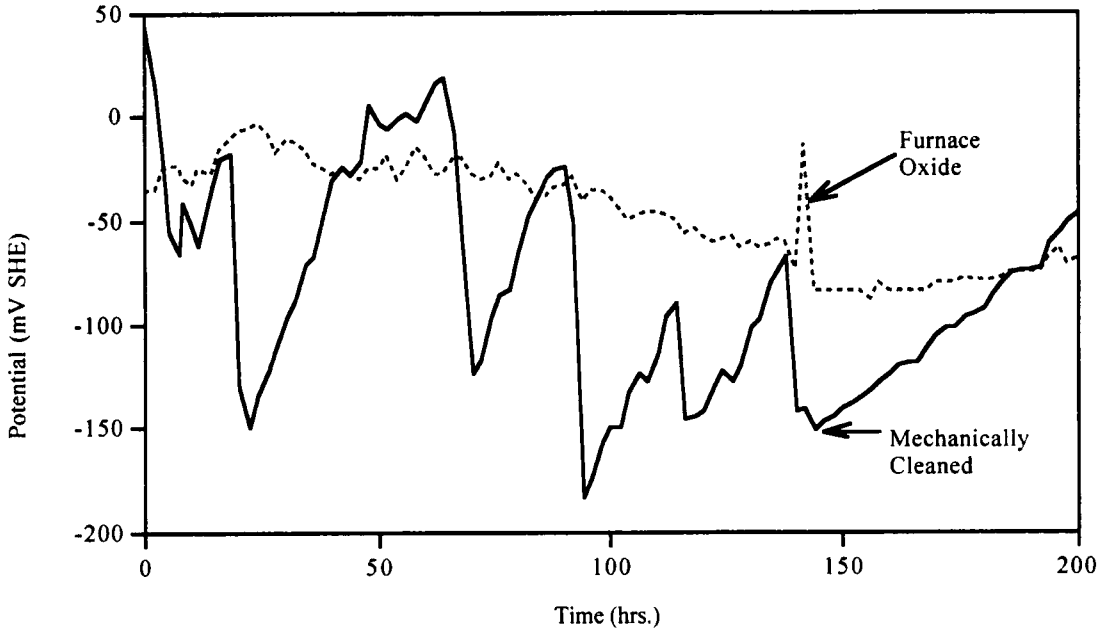

Figure 35: Free corrosion potentials for FAPY during 200-hour U-bend tests.

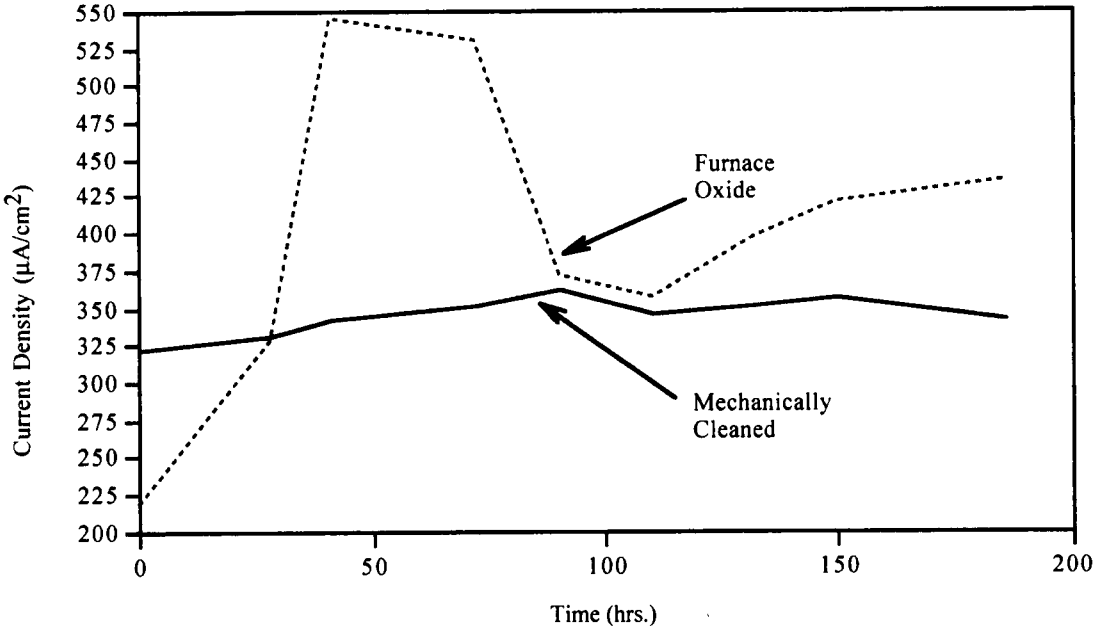

Figure 36: Cathodic current densities for 200-hour U-bend tests at -1500 mV SHE for FAPY specimens.

4.2. 1000°C Furnace Oxide vs. Mechanically Cleaned Surface

4.2.1 Polarization Results

4.2.1.1. FAL

Results for the FAL mechanically cleaned and 1000°C furnace oxide surfaces are shown in Figure 37. It is seen that the mechanically cleaned surface had more resistance to localized corrosion than did the 1000°C furnace oxide surface. The mechanically cleaned surface had a lower value of E_{corr} while having a higher value of $E_{b,pit}$. The mechanically cleaned surface also had a more stable passive current density. This result would suggest that the oxide surface may have been experiencing localized corrosion even while the anodic sweep was still in the passive regime. This could be caused by cracks in the oxide. The cracks could extend to the base material and thereby create a suitable geometry to promote crevice corrosion. This effect would accelerate the onset of localized corrosion as $E_{b,crev}$ (the potential at the onset of crevice corrosion) is usually less than $E_{b,pit}$.

4.2.1.2. FAL-Mo

Results for the 1000°C furnace oxide surface and the mechanically cleaned surface are shown in Figure 38. The oxide surface had very little resistance to localized corrosion especially when compared to the mechanically cleaned surface. In fact, it appears as though the oxide surface has no resistance to pitting corrosion at all. A pit should initiate soon after exposure and freely propagate until the specimen is removed from the corrosive environment. A likely reason for the decreased resistance to pitting corrosion

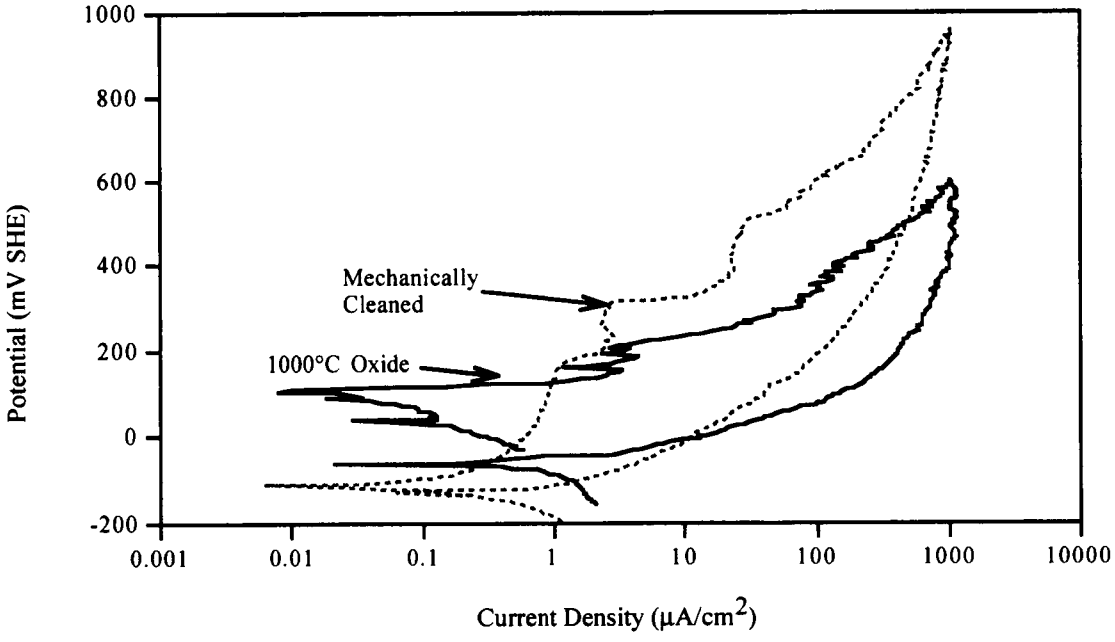

Figure 37: Comparison of 1000°C furnace oxide and mechanically cleaned surfaces of FAL.

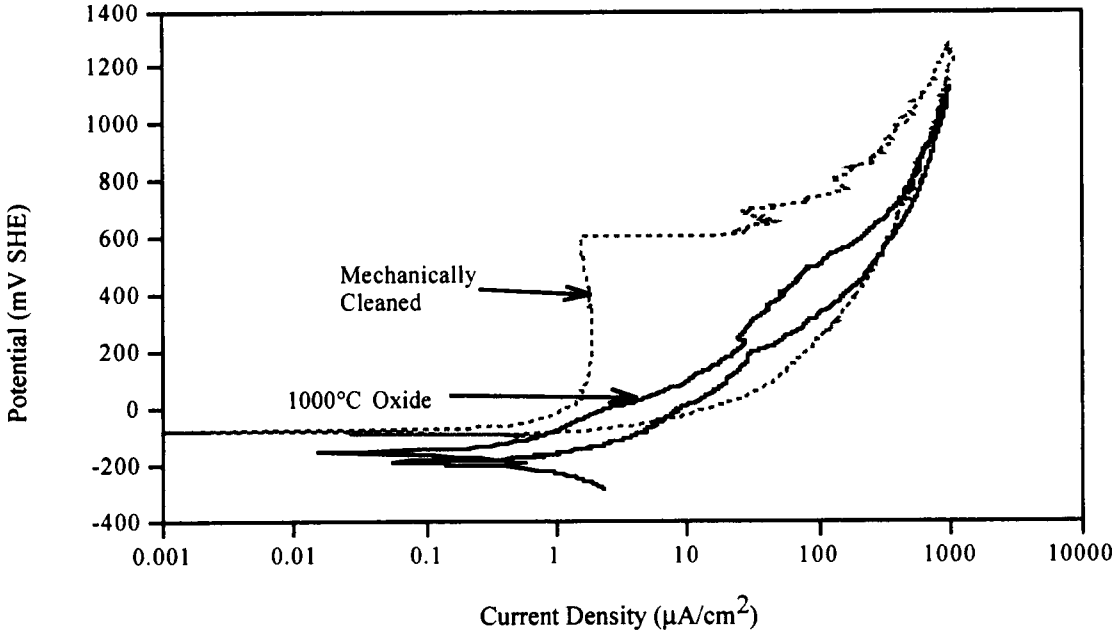

Figure 38: Comparison of 1000°C furnace oxide and mechanically cleaned surfaces of FAL-Mo.

could be caused by the surface topography. Cracks in the oxide may extend down to the base metal. These cracks would have a geometry that is conducive to crevice corrosion. This would thereby make the samples more susceptible to localized corrosion.

Figure 39 shows the comparison of the 750°C and 1000°C furnace oxide surfaces of FAL-Mo. Except for the difference in range of potential, the two oxides behaved similarly. Both had low resistance to localized corrosion.

4.2.1.3. FA-129

The polarization test results for the 1000°C furnace oxide and the mechanically cleaned surfaces of FA-129 are shown in Figure 40. The mechanically cleaned surface greatly outperformed the 1000°C furnace oxide surface. The oxide surface showed no resistance to localized corrosion. One possible explanation for the low resistance to localized corrosion of the oxide surface could be the surface topography. Cracks in the oxide may form a very favorable crevice geometry. This would make the oxide samples more susceptible to localized corrosion.

Figure 41 compares the polarization behaviors of the 750°C furnace oxide surface and the 1000°C furnace oxide surface of FA-129. The two oxides had similar behavior even though they existed at different potentials. Both exhibited relatively no difference between E_{corr} and $E_{b,pit}$.

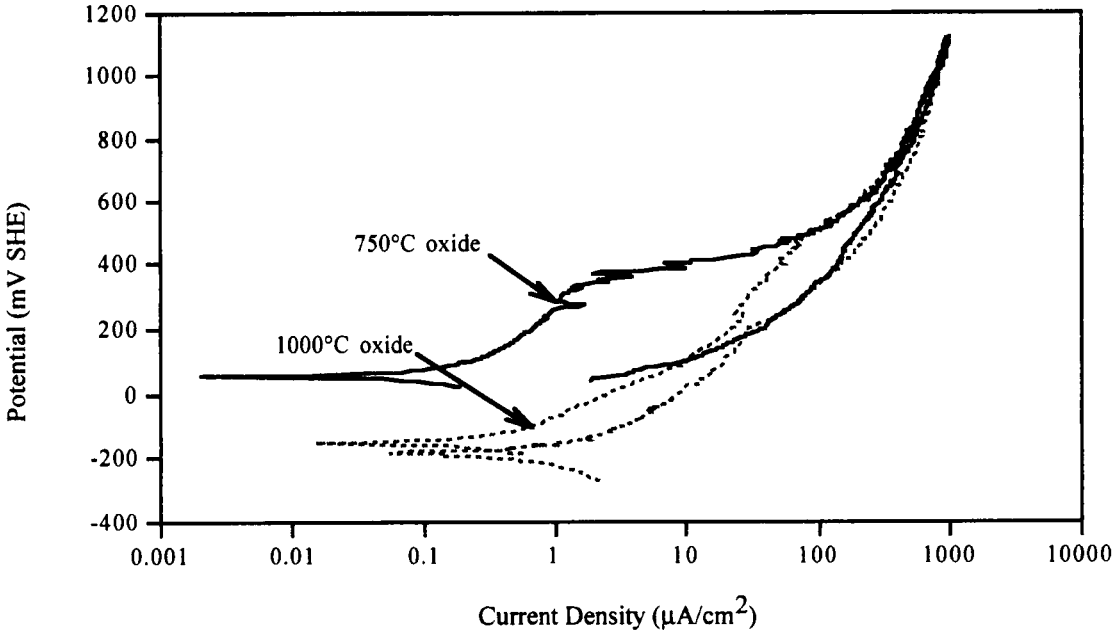

Figure 39: Comparison of 750°C and 1000°C furnace oxide surfaces of FAL-Mo.

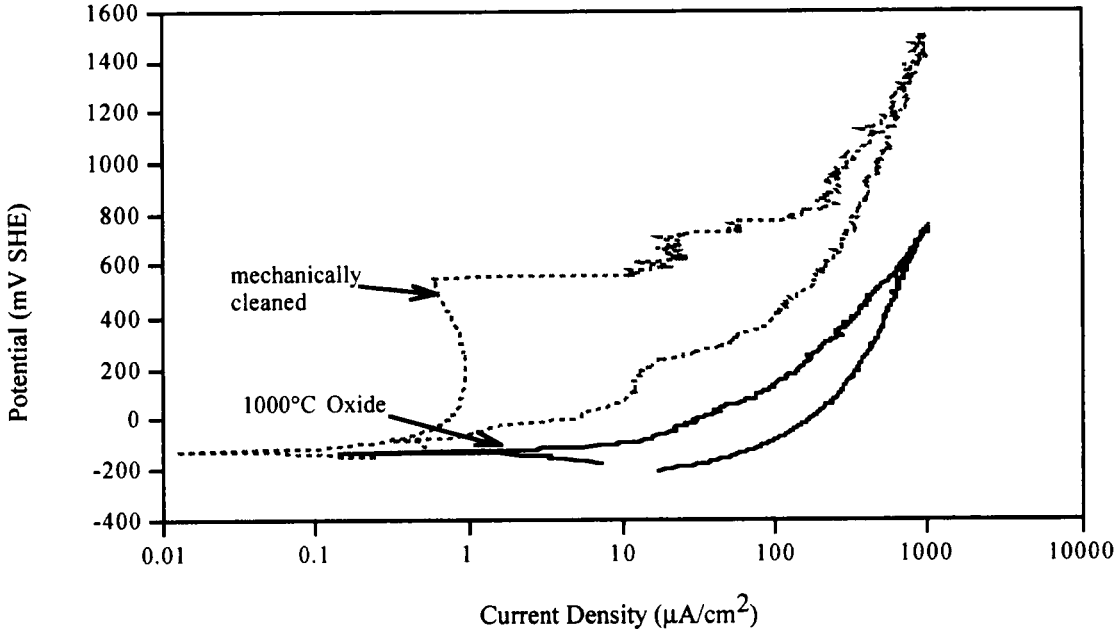

Figure 40: Comparison of 1000°C furnace oxide and mechanically cleaned surfaces of FA-129.

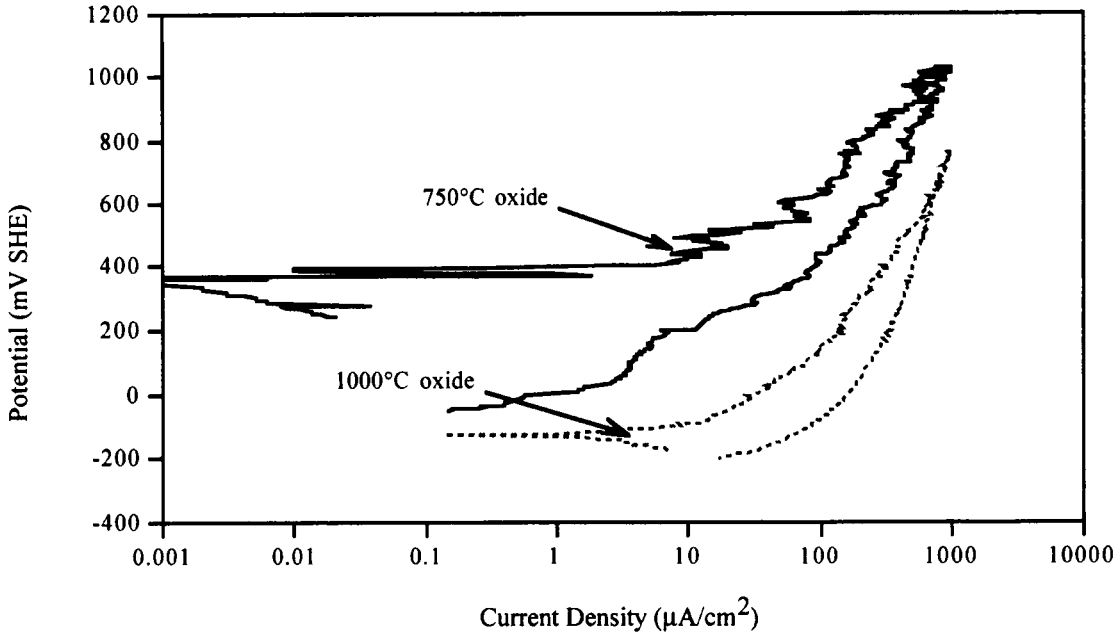

Figure 41: Comparison of the 750°C and 1000°C furnace oxide surfaces of FA-129.

4.2.2. Embrittlement (Slow Strain-Rate Testing) Results

A problem was encountered during the slow strain-rate testing which must be discussed before presenting the valid results. Values of strain obtained from the test were invalid. The primary reason is the method employed to measure the strain. The actual elongation of the sample gage section was not measured. Rather, the crosshead displacement was measured. The crosshead displacement rate was a constant value, thereby making the displacement a linear function of time. The load frame contained several mechanical linkages that had to be tightened before slippage in the system would eliminated. However, the loads employed during the tests were less than 100 pounds and these low values were not sufficient to remove all of the slippage from the mechanical linkages. In order to verify the nature of the problem, a slow strain-rate test was conducted in air on a strip of plain carbon steel. The crosshead displacement was divided by specimen length as an estimate of strain. The resultant stress-strain curve is shown in Figure 42. The known modulus of elasticity for iron based alloys is approximately 30 x 10^6 psi. However, the calculated modulus from Figure 42 is about 1 x 10^6 psi. The discrepancy is too large to be caused by material flaws. Load was eliminated as a cause of the discrepancy because the load cell was in series with the sample. Therefore, any load applied to the sample was also applied to the load cell.

Slow strain-rate data were collected for each iron aluminide sample in the form of load versus time, crosshead displacement versus time, and either corrosion potential or cathodic current density versus time. A representative iron aluminide stress versus time

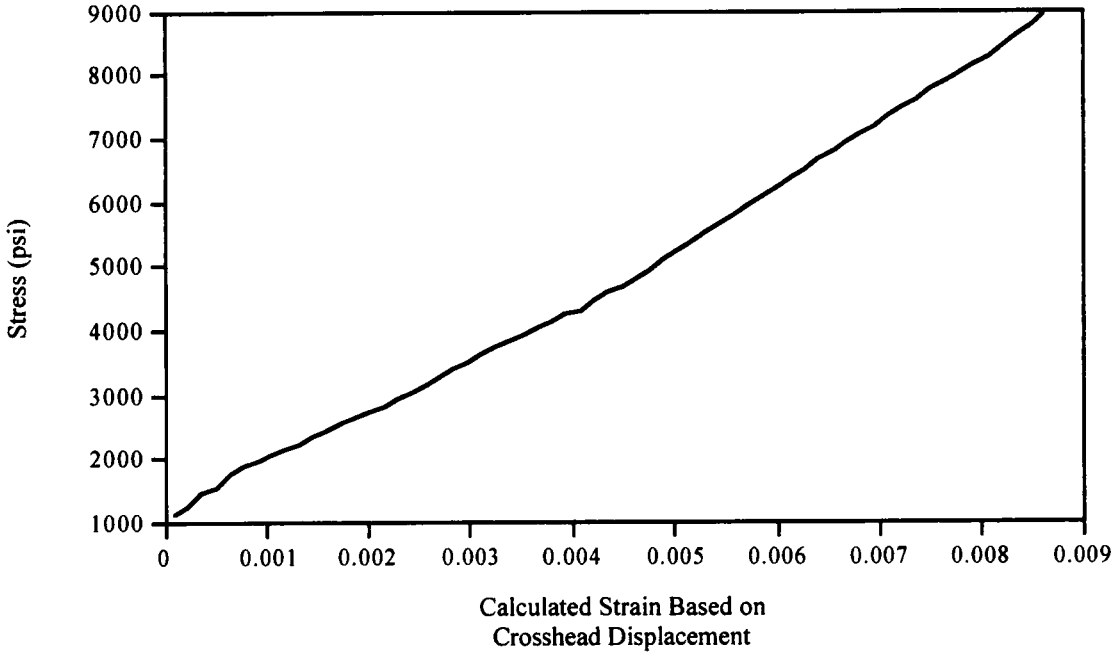

Figure 42: Slow strain-rate test of a plain carbon steel strip.

plot (mechanically cleaned FA-129 at -1500 mV SHE) is shown in Figure 43. This data set was then converted to stress versus strain data, as shown in Figure 44, by dividing the crosshead displacement by the gage length of the sample to determine the calculated strain. The modulus of elasticity that is calculated from Figure 44 is approximately 750,000 psi. The stress versus time curve obtained in Figure 43 matches results obtained in earlier studies by Kim (3). This, therefore, leaves the strain as the factor causing the error in the modulus of FA-129.

Because of the problems associated with the measurement of strain during the slow strain-rate test, the results will not be reported with respect to strain. However, strain is not vital to this study since the effect that surface condition has on the embrittlement of the iron aluminides is of importance here. Therefore, comparisons of alloys with different surface conditions lead to conclusions concerning the effect of surface condition. Since ductility is a major concern, the percent total plastic elongation, as well as the fracture stress, were measured and reported for each test. The total plastic elongation was obtained by placing the two broken parts of the slow strain-rate sample back together, measuring the change in distance between gage marks made on the sample and dividing this change by the original gage length.

The percent total plastic elongation and fracture stress values for the slow strain-rate tests on the iron aluminides are shown in Table 3. The average values are shown in Table 4. The results are summarized in graphical form in Figures 45 and 46.

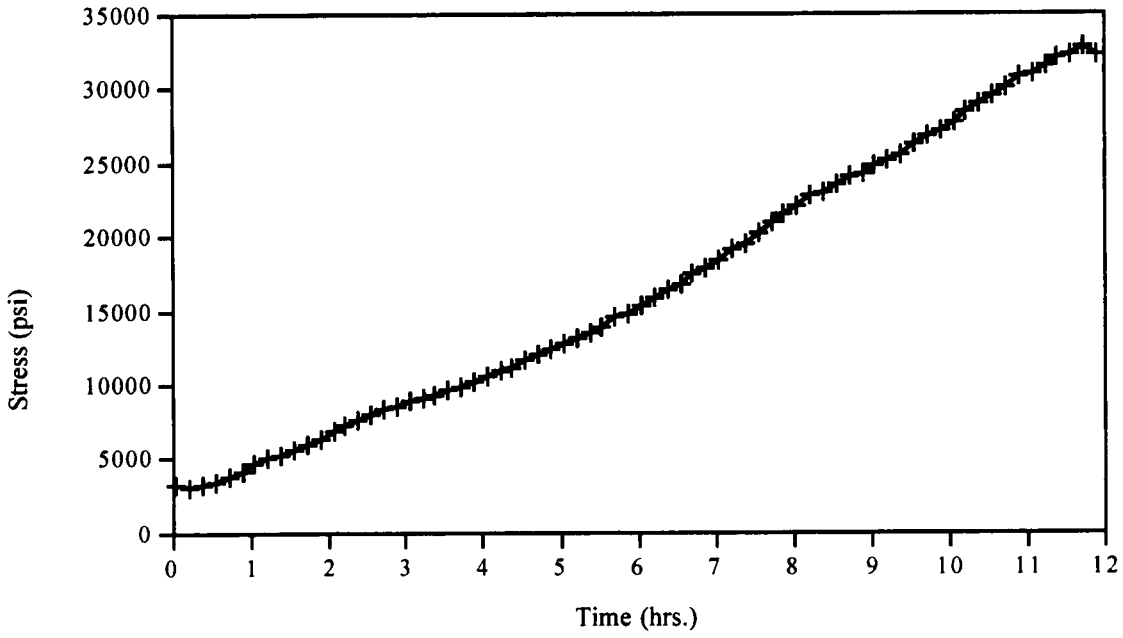

Figure 43: Stress versus time plot for mechanically cleaned sample of FA-129 at -1500 mV SHE.

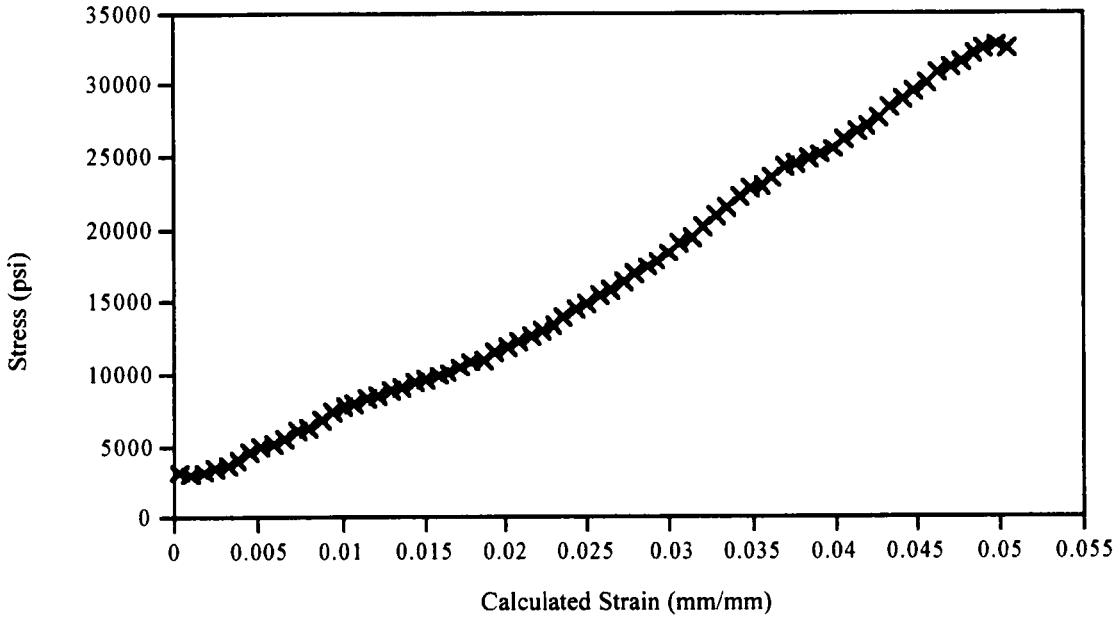

Figure 44: Stress versus calculated strain plot for mechanically cleaned sample of FA-129 at -1500 mV SHE.

Table 3: Results of slow strain-rate tests on iron aluminides.

Material	Potential	Surface Condition	Fracture Stress [ksi (MPa)]		Percent Total Plastic Elongation
FAL	E_{corr}	Mechanically Cleaned	22	150	2.23
		Mechanically Cleaned	27	183	3.13
		1000°C Furnace Oxide	24	163	3.32
		1000°C Furnace Oxide	26	177	3.76
	-1500 mV SHE	Mechanically Cleaned	21	143	1.42
		Mechanically Cleaned	25	170	1.72
		1000°C Furnace Oxide	19	129	2.23
		1000°C Furnace Oxide	23	156	2.49
FAL-Mo	E_{corr}	Mechanically Cleaned	30	204	1.09
		Mechanically Cleaned	38	258	1.27
		1000°C Furnace Oxide	24	163	1.52
		1000°C Furnace Oxide	30	198	1.62
	-1500 mV SHE	Mechanically Cleaned	40	272	1.92
		Mechanically Cleaned	48	326	2.02
		1000°C Furnace Oxide	34	231	3.87
		1000°C Furnace Oxide	38	254	3.95
FA-129	E_{corr}	Mechanically Cleaned	35	238	1.71
		Mechanically Cleaned	39	261	1.83
		1000°C Furnace Oxide	31	211	2.72
		1000°C Furnace Oxide	37	251	2.80
	-1500 mV SHE	Mechanically Cleaned	29	197	1.12
		Mechanically Cleaned	35	239	1.24
		1000°C Furnace Oxide	23	156	1.23
		1000°C Furnace Oxide	25	170	1.29

Table 4: Average results of slow strain-rate tests on iron aluminides.

Material	Potential	Surface Condition	Average Fracture Stress [ksi (MPa)]	Average Percent Total Plastic Elongation
FAL	E_{corr}	Mechanically Cleaned	25 172	2.76
		1000°C Furnace Oxide	25 173	3.54
	-1500 mV SHE	Mechanically Cleaned	23 164	1.57
		1000°C Furnace Oxide	21 146	2.36
FAL-Mo	E_{corr}	Mechanically Cleaned	34 237	1.18
		1000°C Furnace Oxide	27 190	1.57
	-1500 mV SHE	Mechanically Cleaned	44 305	1.97
		1000°C Furnace Oxide	36 252	3.91
FA-129	E_{corr}	Mechanically Cleaned	37 256	1.77
		1000°C Furnace Oxide	34 235	2.76
	-1500 mV SHE	Mechanically Cleaned	32 223	1.18
		1000°C Furnace Oxide	24 165	1.26

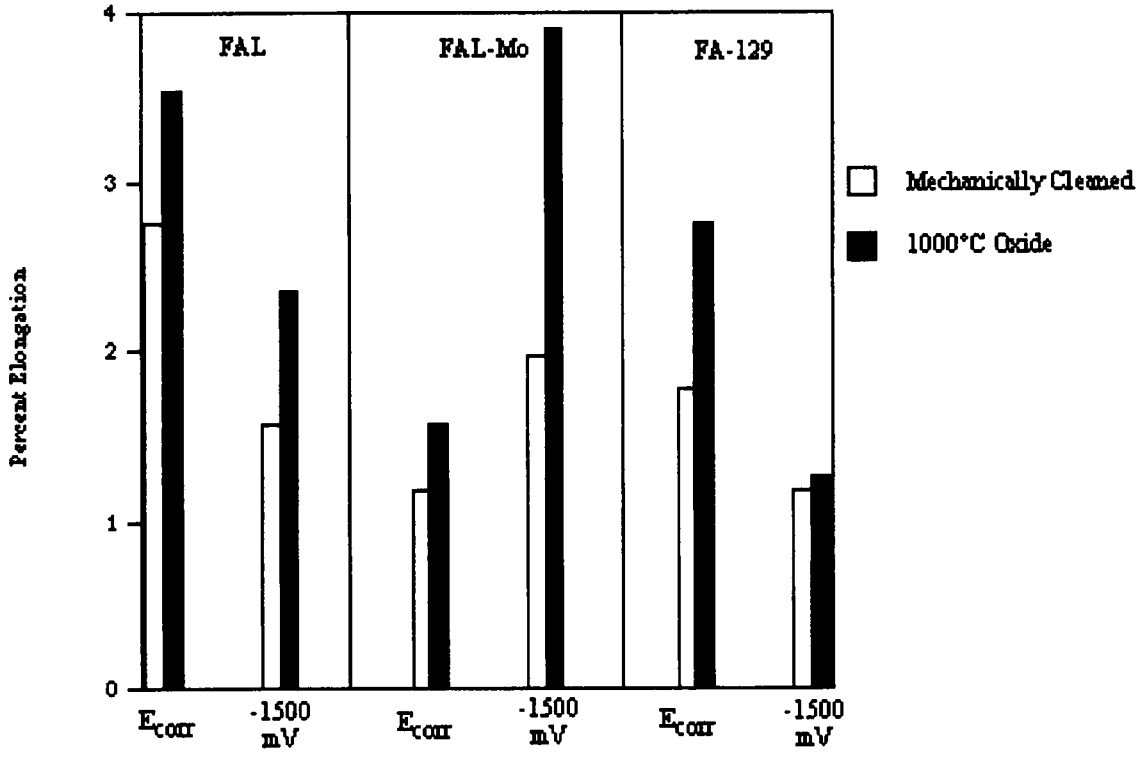

Figure 45: Percent total plastic elongation of iron aluminides during slow-strain rate test.

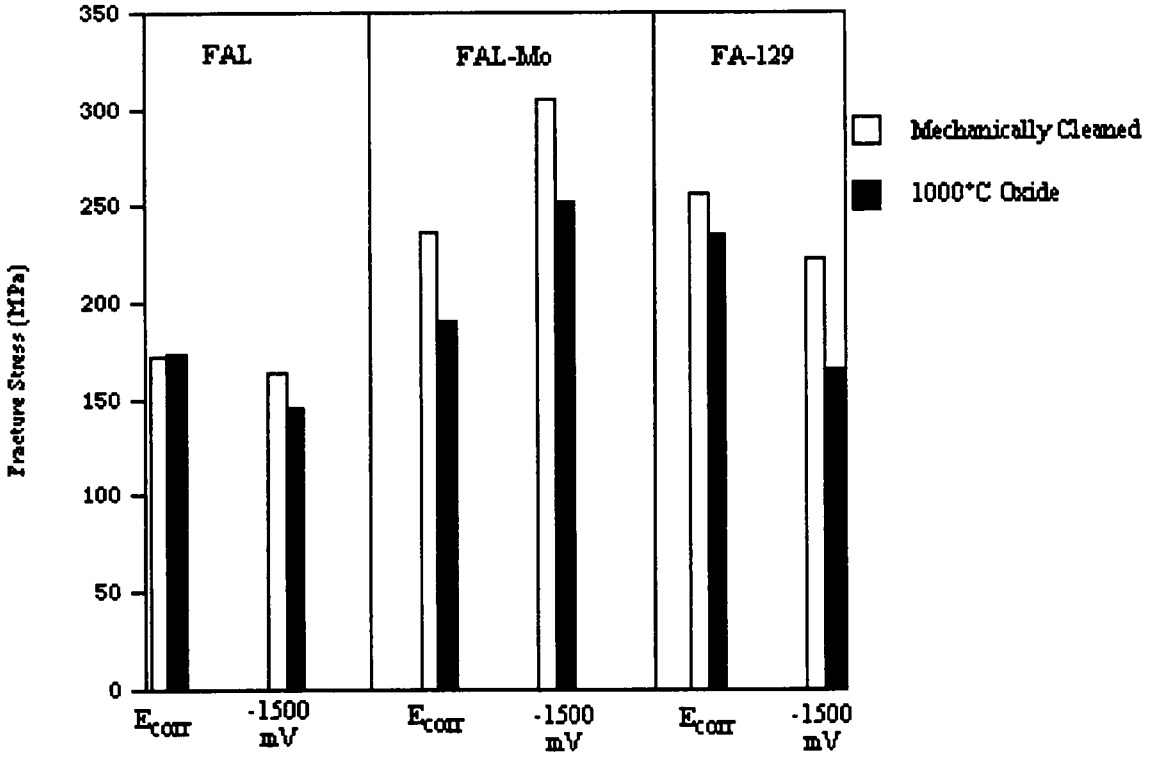

Figure 46: Fracture stresses of iron aluminides during slow-strain rate tests.

4.2.2.1. FAL

It was shown in Figures 45 and 46 that for FAL at E_{corr} the mechanically cleaned surface had a lower percent elongation and a nearly equal fracture stress. Figure 47 shows the corrosion potential versus time plot for the FAL during the slow strain-rate test at E_{corr}. The corrosion potential for the 1000°C furnace oxide surface was higher than for the mechanically cleaned surface. The potential plot gives no clear indication that either sample underwent pitting and no signs of pitting were found visually. Since there was no sign of pitting, there is no reason to suspect that the 1000°C furnace oxide sample was subjected to stress concentration effects that would be caused by pits. With pitting effects being equal for both samples, the only real difference is surface condition. Since the percent total plastic elongation was greater for the 1000°C furnace oxide surface, then the amount of plasticity was greater. In other words, the mechanically cleaned specimen was embrittled in comparison to the oxide specimen. Therefore, at E_{corr}, the 1000°C furnace oxide provided some protection against hydrogen penetration into the base material.

At -1500 mV SHE, the mechanically cleaned sample had a lower percent total plastic elongation with a higher fracture stress than the 1000°C furnace oxide sample. The fact that the percent total plastic elongation was lower for the mechanically cleaned sample indicates that there was embrittlement when compared to the 1000°C furnace oxide sample. Also, the greater fracture stress indicates less tendency for slip to occur and relieve the stress in the sample. Finally, as shown in Figure 48, the cathodic current

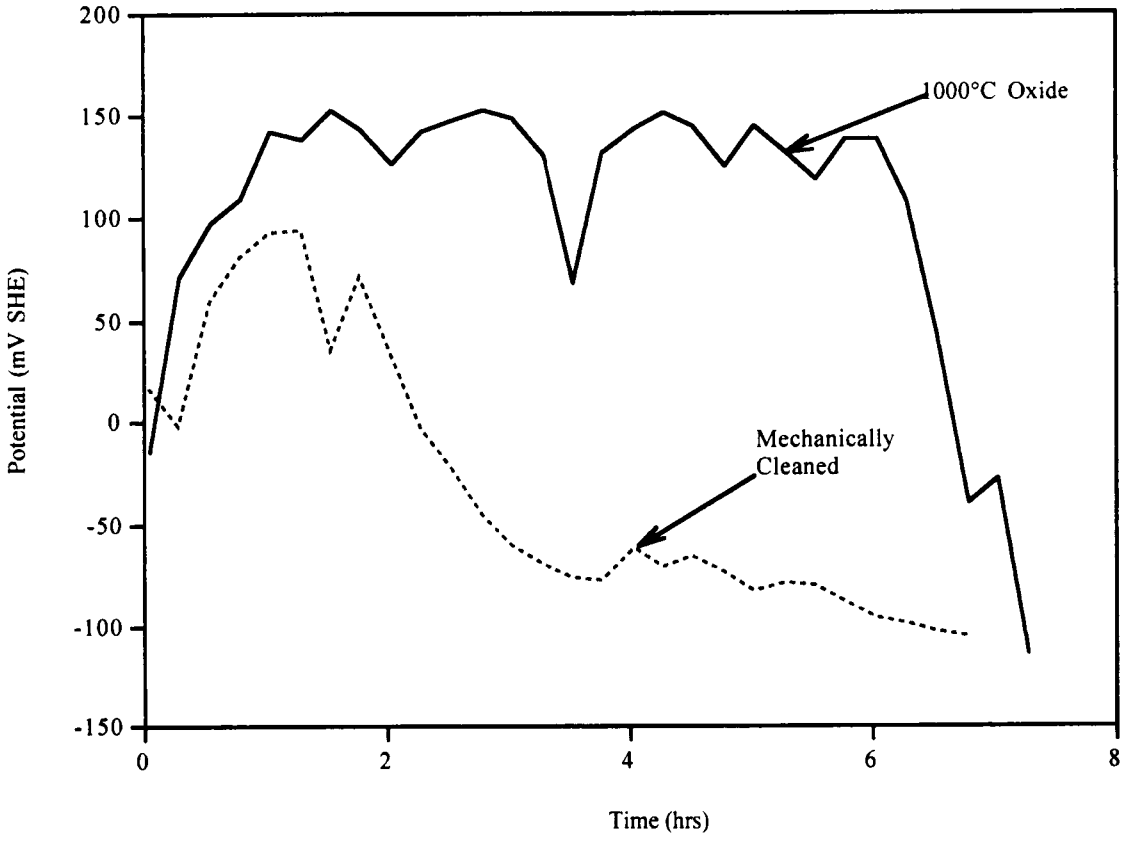

Figure 47: Corrosion potential versus time for slow strain-rate samples of FAL.

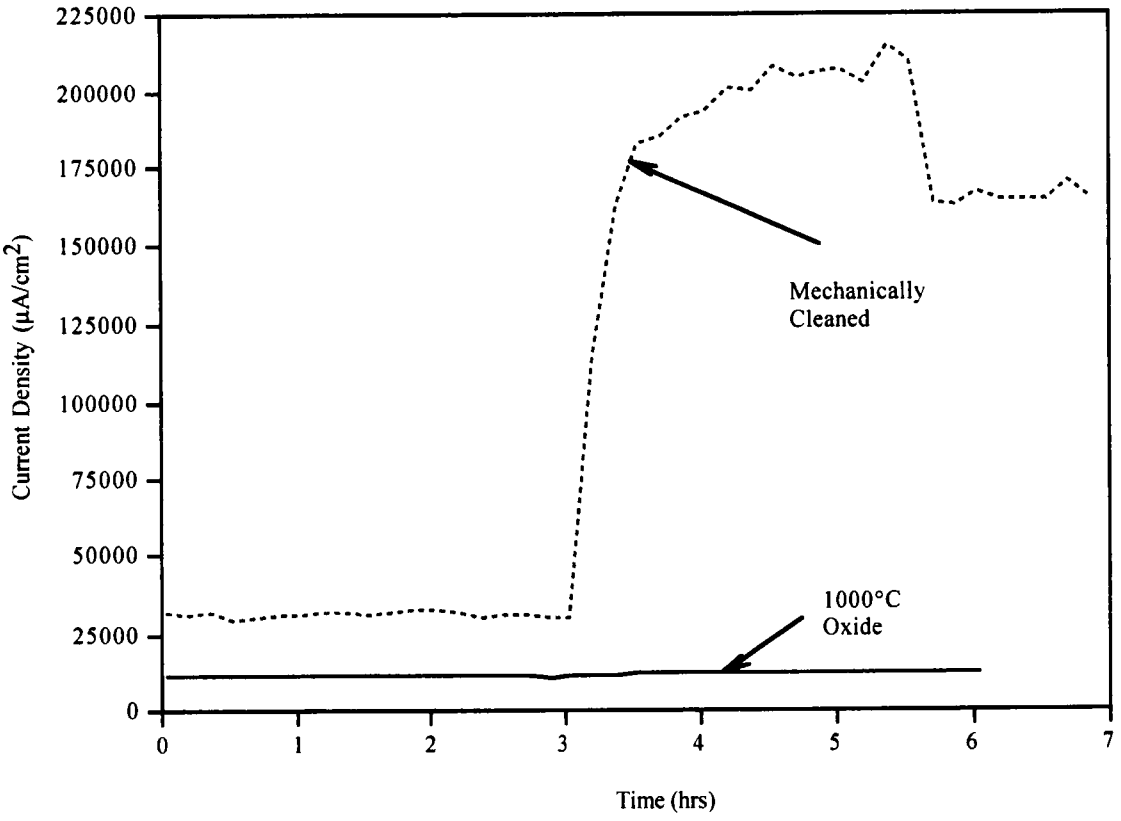

Figure 48: Cathodic current density versus time at -1500 mV SHE for slow strain-rate samples of FAL.

density for the 1000°C furnace oxide sample was lower than the current density for the mechanically cleaned sample. This suggests that the oxide surface not only provides protection against hydrogen penetration but also retards hydrogen production on the surface of the specimen. All of this indicates that the oxide has a beneficial effect on the slow strain-rate properties.

4.2.2.2. FAL-Mo

Figures 45 and 46 show that for the mechanically cleaned surface of FAL-Mo the percent total plastic elongation was lower while the fracture stress was higher than the 1000°C furnace oxide sample at both E_{corr} and -1500 mV SHE. Figure 49 shows the corrosion potential versus time for the two samples of FAL-Mo at E_{corr}. It can be seen that neither sample showed any signs of pit initiation occurring by sharp peaks in the potential curves. Therefore, neither sample experienced stress concentrations due to pit formation. With this effect being equal in both samples, the results suggest that the oxide surface is providing more protection than the mechanically cleaned surfaces from hydrogen penetration and subsequent hydrogen embrittlement.

Figure 50 shows the cathodic current density at -1500 mV SHE versus time for the slow strain-rate samples of FAL-Mo. It can be seen that initially the cathodic current density was higher for the mechanically cleaned sample. It was also greater at the time of fracture. This suggests that, during these time periods, the oxide retarded hydrogen production on the surface of the sample. This would provide added protection against hydrogen embrittlement.

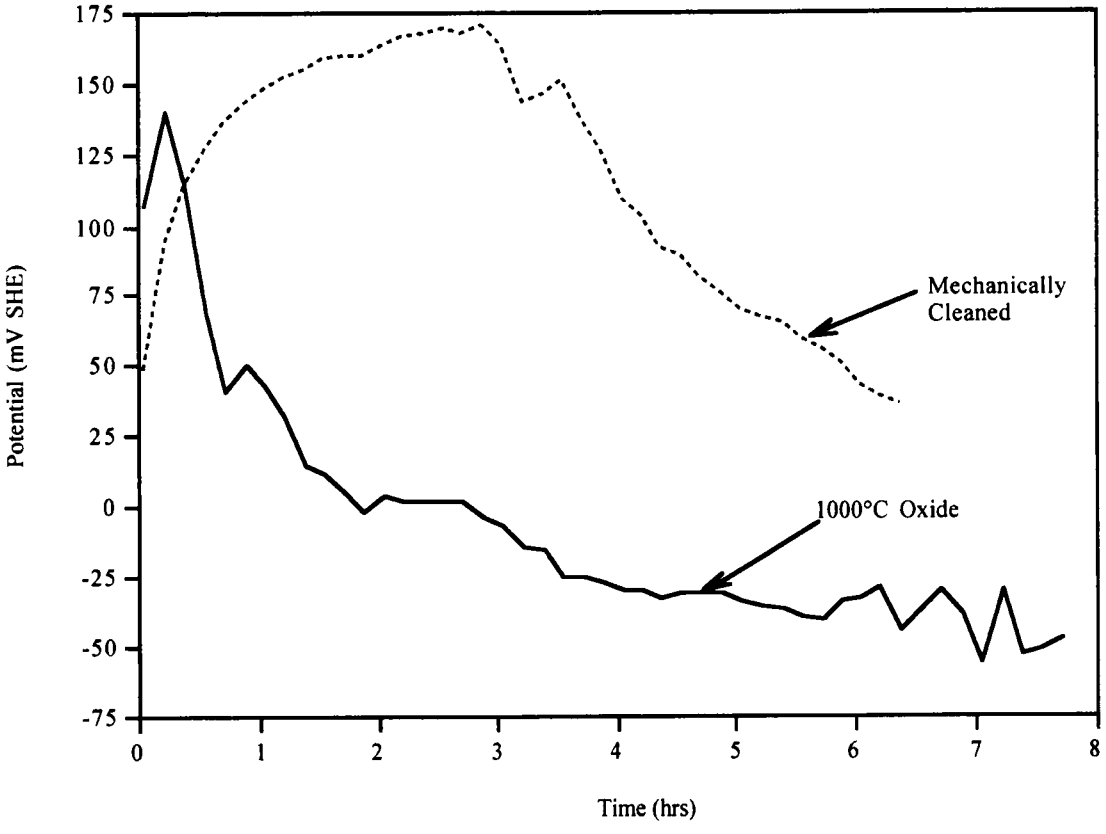

Figure 49: Corrosion potential versus time for slow strain-rate samples of FAL-Mo.

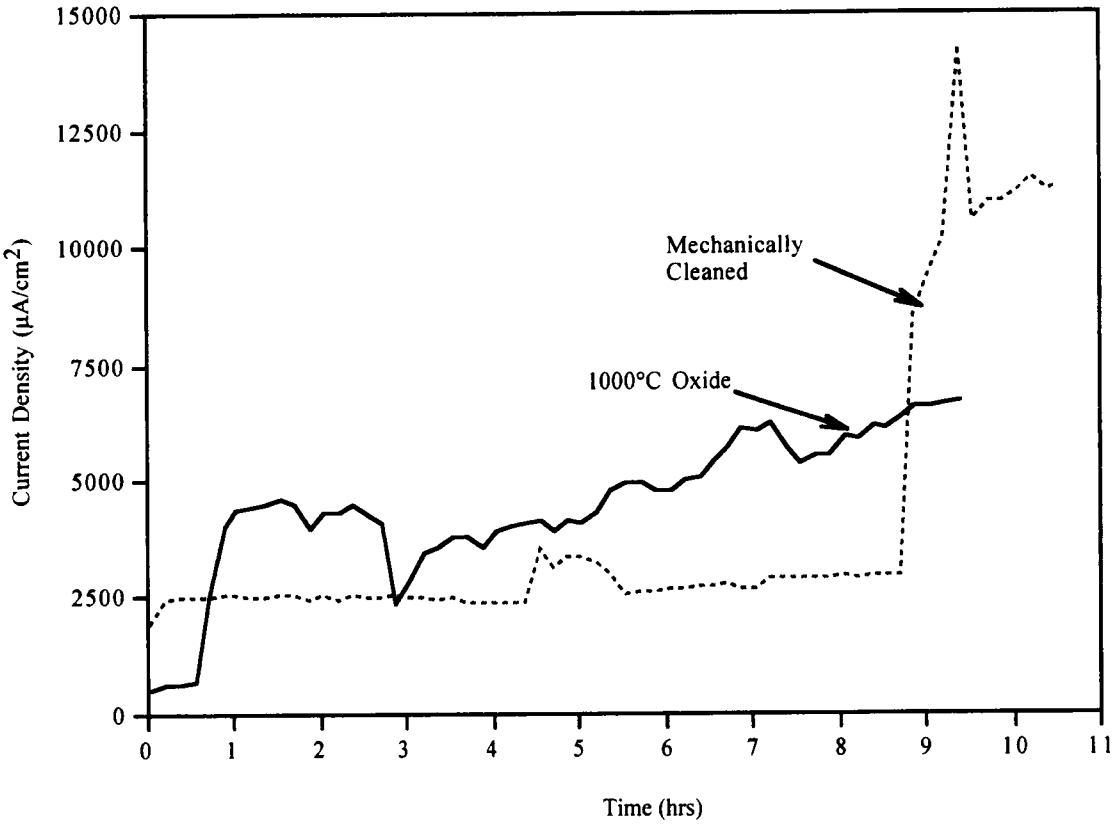

Figure 50: Cathodic current density versus time at -1500 mV SHE for slow strain-rate samples of FAL-Mo.

4.2.2.3. FA-129

Figures 45 and 46 showed that the mechanically cleaned samples of FA-129 had lower percents total plastic elongation and higher fracture stresses than did the 1000°C furnace oxide samples at both E_{corr} and -1500 mV SHE. Figure 51 shows the corrosion potential versus time for the slow strain-rate samples of FA-129. The potential for the mechanically cleaned surface was lower for most of the test, but neither sample appeared to be experiencing localized corrosion. However, after the test was completed, both samples had corrosion products on the surface. No pits were observed on the fracture surfaces of the samples. In the absence of pits to act as stress concentration sites, then the factor causing loss of ductility in the mechanically cleaned sample must be hydrogen related. Therefore, the oxide provides some protection again hydrogen penetration into the 1000°C furnace oxide sample.

Figure 52 shows the cathodic current density at -1500 mV SHE versus time for the slow strain-rate samples of FA-129. It is seen that the cathodic current density for the furnace oxide sample was higher than for the mechanically cleaned surface. Despite this, the oxide sample had a slightly higher percent total plastic elongation. The fact that the samples behaved similarly with respect to ductility could be due to the oxide on FA-129 not being as adherent as it was on FAL or FAL-Mo.

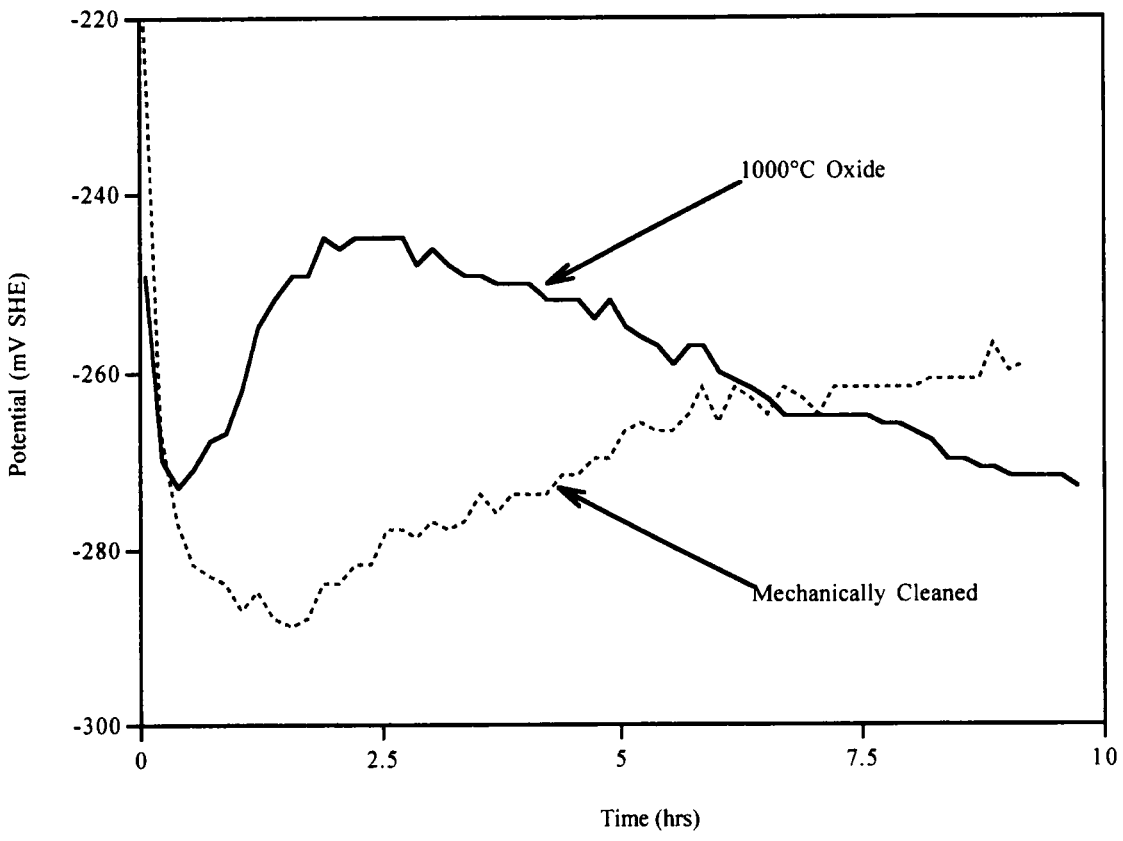

Figure 51: Corrosion potential versus time plot for slow strain-rate samples of FA-129.

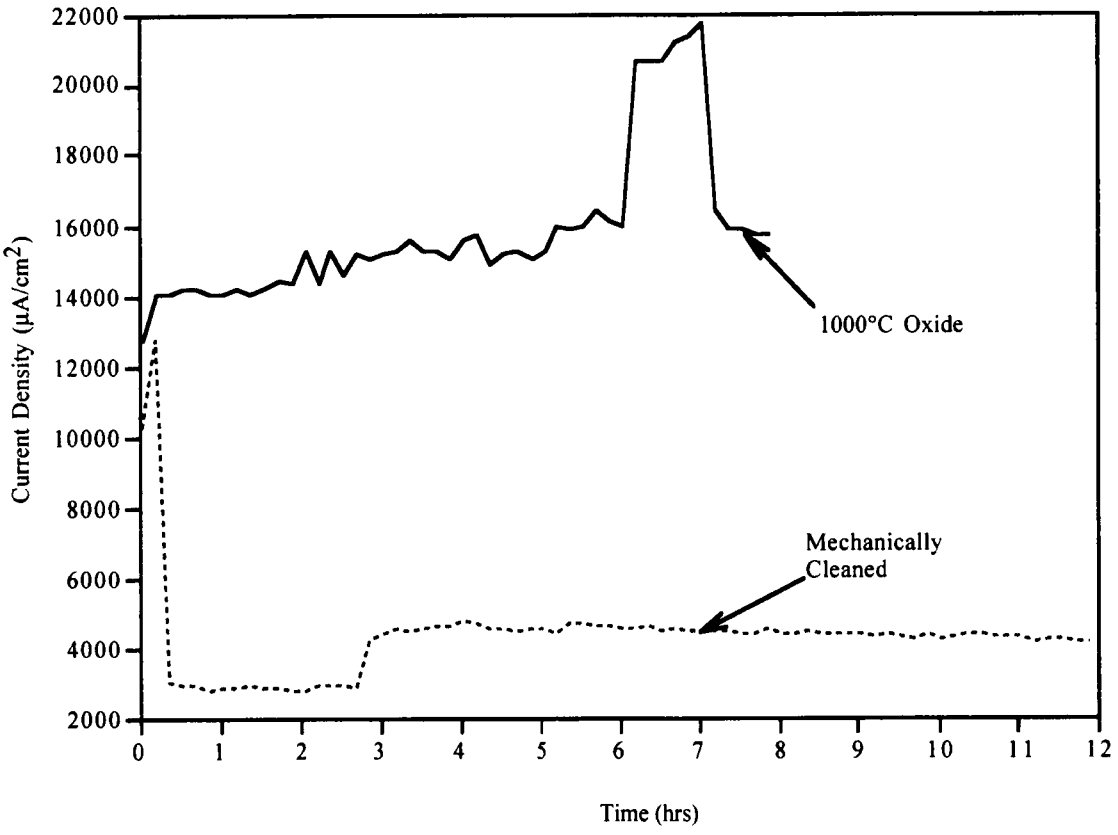

Figure 52: Cathodic current density versus time at -1500 mV SHE for slow strain-rate samples of FA-129.

4.2.2.4. Fractography

In addition to the data collected during the slow strain-rate tests, it was desirable to determine the mode of cracking that led to failure. Therefore, fractography by scanning electron microscopy was performed. Since hydrogen embrittlement was believed to be involved, intergranular fracture, cleavage, or quasi-cleavage should be found on the fracture surface. A typical fractograph for all of the samples is shown in Figure 53. It can be seen that the fracture surface features were very similar in shape and size to the grain structure, which is shown in Figure 54. The size of the grains in Figure 53 is very close to the size of the grains shown in Figure 54. The fracture surface is indicative of intergranular brittle fracture which is consistent with hydrogen embrittlement of the slow strain-rate specimens.

Figure 53: Fracture surface of 1000°C furnace oxide sample of FAL slow strain-rate specimen tested at -1500 mV SHE.

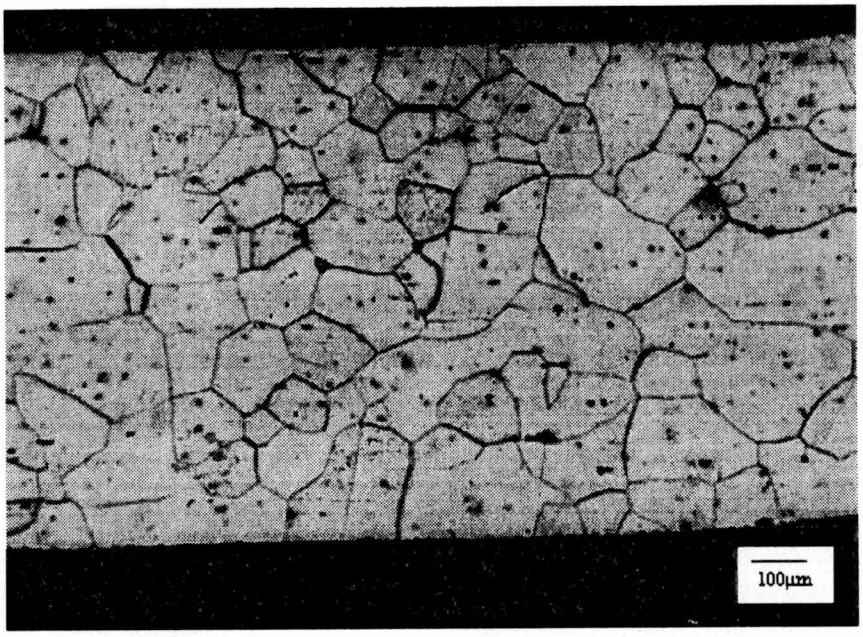

Figure 54: Annealed microstructure of FAL slow strain-rate specimen.

V. Summary of Results and Conclusions

The results and conclusions of this study are summarized as follows:

5.1 As-Processed and 750°C Furnace Oxide Surfaces Versus Cleaned Surfaces

Polarization results

Polarization tests in a mild acid-chloride solution for all alloys showed that E_{corr} was higher for the as-processed and 750°C furnace oxide samples than for the mechanically or chemically cleaned samples. Also, $E_{b,pit}$ was lower for the two oxide surfaces than for the two cleaned surfaces. Therefore, the pitting corrosion resistance was shown to be lower for the oxide surfaces than for the cleaned surfaces. Comparisons of the 750°C furnace oxide samples and as-processed samples indicated similar polarization behavior. The differences in corrosion characteristics between the oxide and cleaned samples is believed to be caused by surface morphology. Whereas the relative smooth surface finishes of the cleaned samples precluded crevice-type flaws, the oxide samples likely contained cracks or other flaws in the oxides which were conducive to crevice corrosion.

Embrittlement results

U-bend tests for 200 hours in the mild acid-chloride solution were conducted for alloys with mechanically cleaned and 750°C furnace oxide surfaces. None of the samples, with either surface condition, fractured when tested at the free corrosion potential. However, at the hydrogen charging potential of -1500 mV SHE, samples of FA-84, FAL-Mo, and FA-129 fractured in the mechanically cleaned condition only.

None of the oxide samples fractured at the hydrogen charging potential. This result indicated that under static loading conditions, hydrogen embrittlement was minimized by the presence of the 750°C furnace oxide, which hindered hydrogen penetration to such a point that fracture did not occur during the 200 hour tests.

5.2. 1000°C Furnace Oxide Surfaces Versus Mechanically Cleaned Surfaces

Polarization results

The 1000°C furnace oxide surfaces for all alloys performed poorly with respect to the mechanically cleaned surfaces. The 1000°C furnace oxide surfaces showed nearly no resistance to localized corrosion. It is believed that this result was caused by the surface morphology of the oxide samples which was conducive to crevice corrosion. Cracks in the oxide structure would provide narrow yet relatively long geometries that would promote crevice corrosion.

Embrittlement results

Slow strain-rate tests were conducted on samples with 1000°C furnace oxide and mechanically cleaned surfaces. The oxide samples had higher percent total plastic elongations, while having lower fracture strengths. The mechanically cleaned samples, therefore, had lost some plasticity and had become embrittled relative to the oxide samples. The results indicated that the oxide surfaces hindered hydrogen penetration into the materials and thereby retarded hydrogen embrittlement effects.

Bibliography

1. V. K. Sikka, SAMPE Quarterly, 22, no. 4, p. 2-10 (1991)

2. C. G. McKamey, P. J. Maziasz, G. M. Goodwin, T. Zacharia, Materials Science and Engineering, A174, pp. 59-70, (Jan 1994).

3. J. G. Kim, Ph.D. Dissertation, University of Tennessee, Knoxville (1992).

4. J. G. Kim, R. A. Buchanan, Corrosion, pp. 658-668 (Sept. 1994)

5. Binary Alloy Phase Diagrams Vol. 1, T. B. Massalski, ed., American Society of Metals, Metals Park, OH (1986).

6. S. M. Allen, J. W. Cahn, Acta Metallurgica, **23**, pp. 1017-1026 (1975).

7. P.R. Swann, W. R. Duff, Trans. of the Metall. Soc. of AIME, 245, p. 851 (1969).

8. H. Okamoto, P. A. Beck, Metall. Trans., 2, p. 569 (1971).

9. Z. Q. Sun, Y. D. Huang, W. Y. Yang, G. L. Chen, Materials Research Symposium Proceedings, **288**, pp. 885-890, (1993).

10. C. T. Liu, C. G. McKamey, E. H. Lee, Scripta Metallurgica, **24**, pp. 385-390 (1990).

11. T. Takasugi, ACTA Metall., 31 (8), p. 1187 (1983).

12. C. G. McKamey, V. K. Sikka, Fossil Energy Advanced Research and Technology Development Materials Program, Semiannual Progress Report for the Period Ending, ORNL/FMP-89/1, p. 267 (1989).

13. C. G. McKamey, V. K. Sikka, Fossil Energy Advanced Research and Technology Development Materials Program, Semiannual Progress Report for the Period Ending, ORNL/FMP-90/2, p. 235 (1990).

14. C. G. McKamey, Met. Trans. A, 20A, p. 751 (1989).

15. J. R. Galvele, J. Electrochemical Society, **123**, No. 4, pp. 464-474 (April 1976).

16. E. E. Stansbury, R. A. Buchanan, Fundamentals of Electrochemical Corrosion, University of Tennessee, Knoxville, (1993).

17. H. Kaesche, Metallic Corrosion, NACE, p. 90 (1985)

18. R. H. Jones, R. E. Ricker, in Stress-Corrosion Cracking Materials Performance and Evaluation, R. H. Jones ed., ASMI, (1992).

19. J. J. DeLuccin, in Hydrogen Embrittlement: Prevention and Control, L. Raymond Ed., STP 962, p. 17 (1988)

20. C. A. Zappfe, C. E. Sims, Trans. AIME, **145**, p 225 (1941).

21. R. P. Frohmberg, W. J. Barnelt, and A.R. Troiano, Trans. AIME, 47, p. 892 (1955)

22. A. R. Troiano, Trans. AIME, 52, p. 54 (1960)

23. M. O. Speidel, in Hydrogen Embrittlement and SCC, R. Gibala, Ed., ASM, pp. 271 (1984).

24. ASTM Standards G61-86, 03.02, pp. 238-241 (1986).

25. ASTM Standards G30-90, 03.02, pp. 96-101 9 (1990).

26. R. N. Parkins, Corrosion, vol. 46, n. 3, p. 178 (1990)

27. J. A. Beavers, G. H. Koch, Corrosion, vol. 48, n. 3, p. 256-264 (1992)

28. C. D. Kim, B. E. Wilde, in SCC-The Slow strain-rate Technique, G. M Ugiansky, Ed., ASTM STP 665, p. 97 (1979)

29. Z. S. Smialowska, Pitting Corrosion of Metals, NACE, p. 47 (1986)

30. J. H. Payer, W. E. Berry, W. K. Boyd, in SCC-The Slow Strain-Rate Technique, G. M. Ugiansky, Ed., ASTM STP 665, p.68 (1979)

31. ASTM Standards G5-87, 03.02, p. 124 (1987)

32. V. Kerlins, in Metals Handbook, Ninth Ed., ASM, 12, p. 24 (1987)

Vita

Robert L. Perrin was born in Alexandria, Louisiana, on January 17, 1972. He graduated from Northeast High School in Clarksville, Tennessee in May of 1990. In August of 1990, he started his undergraduate work at the University of Tennessee in Knoxville. He received a Bachelor of Science in Materials Science and Engineering in December of 1994. He began his study towards a Master's Degree at the University of Tennessee in Knoxville in January of 1995. He was awarded a Master of Science degree in Metallurgical Engineering on August 9, 1996.